bioRxiv preprint doi: https://doi.org/10.1101/2022.04.05.487130; this version posted April 6, 2022. The copyright holder for this preprint (which was not certified by peer review) is the author/funder, who has granted bioRxiv a license to display the preprint in perpetuity. It is made available under aCC-BY-ND 4.0 International license.

Multiple congenital malformations arise from somatic mosaicism for constitutively active Pik3ca signalling

1 **Elise Marechal [1], Anne Poliard [2], Mathias Moreno [1], Mathilde Legrix [1], Nicolas Macagno [1],**
2 **Grégoire Mondielli [1], Teddy Fauquier [1], Anne Barlier [1,3], Heather C. Etchevers [4*]**

3 [1] Aix Marseille Univ, INSERM, MMG, U1251, MarMaRa Institute, Marseille, France

4 [2] URP 2496 Orofacial Pathologies, Imagery, and Biotherapies, CNRS, GDR 2031 CREST-NET,
5 School of Dentistry, Université Paris Cité, Montrouge, France

6 [3] AP-HM, MMG, MarMaRa Institute, La Conception Hospital Laboratory of Molecular Biology,
7 Marseille, France

8 [4] Aix Marseille Univ, INSERM, MMG, U1251, CNRS, GDR 2031 CREST-NET, MarMaRa
9 Institute, Marseille, France

10 *** Correspondence:**
11 Heather C. Etchevers
12 heather.etchevers@inserm.fr ORCID: 0000-0003-0201-3799

13 **Keywords: neural crest, embryo, PI3K, cancer, birth defect, cleft palate, vascular anomaly**

14 1 Abstract

15 Recurrent missense mutations of the *PIK3CA* oncogene are among the most frequent drivers of
16 human cancers. These often lead to constitutive activation of its product p110α, a
17 phosphatidylinositol 3-kinase (PI3K) catalytic subunit. In addition to causing a range of rare and
18 common cancers, the H1047R mutation is also found in affected tissues of a distinct set of congenital
19 tumours and malformations. Collectively termed *PIK3CA*-related disorders (PRDs), these lead to
20 overgrowth of skin, brain, adipose, connective, musculoskeletal tissues and/or blood and lymphatic
21 vessel components. Vascular malformations are frequently observed in PRD due to cell-autonomous
22 activation of the PI3K signaling pathway within endothelial cells. These, like most muscle,
23 connective tissue and bone, are derived from the embryonic mesoderm. However, important organ
24 systems affected in PRDs are neuroectodermal derivatives. To further examine their development, we
25 drove the most common post-zygotic activating mutation of *Pik3ca* in neural crest and related
26 embryonic lineages. Effects in cells having once expressed Wnt1, including the brain roofplate and
27 most neural crest, were most dramatic in the head. Outcomes included megalencephaly, cleft
28 secondary palate and more subtle skull anomalies. Surprisingly, *Pik3ca*-mutant subpopulations of
29 either mesodermal or neural crest origin was associated with widespread vascular anomalies, leading
30 us to incidentally discover previously undescribed lineages that had expressed the transcription factor
31 Egr2 (Krox20) and that may be co-opted in pathogenesis. Schwann cell precursors having transcribed
32 either Krox20 or Sox10 also gave rise to adult-onset vascular tumors and cancers, including
33 melanoma, after Pik3ca activation. These murine phenotypes may aid discovery of new candidate
34 human PRDs affecting craniofacial and vascular smooth muscle development as well as the
35 reciprocal paracrine signaling mechanisms leading to tissue overgrowth.

bioRxiv preprint doi: https://doi.org/10.1101/2022.04.05.487130; this version posted April 6, 2022. The copyright holder for this preprint (which was not certified by peer review) is the author/funder, who has granted bioRxiv a license to display the preprint in perpetuity. It is made available under aCC-BY-ND 4.0 International license.

36 ## 2 Introduction

37 Inappropriate activation of signaling components between the cell membrane and its nucleus leads to
38 pathologies with onset at any stage of life, ranging from before birth into old age. These include most
39 cancers, but also numerous, individually rare diseases with a congenital basis.

40 Nearly two dozen distinct overgrowth disorders, characterized by somatic mosaicism for gene
41 mutations that constitutively activate the phosphatidylinositol 3-kinase (PI3K) pathway, have been
42 discovered over the last decade (Canaud et al., 2021). A striking majority of these diseases show the
43 same hotspot, activating mutations in the *PIK3CA* gene as found in cancer, which has led to their
44 qualification as PIK3CA-related disorders (PRDs). A large subset is known as "PIK3CA-related
45 overgrowth syndromes" or PROS, where susceptible tissues such as the cortex (Alcantara et al.,
46 2017), skeletal muscles (Frisk et al., 2019) or the face (Couto et al., 2017) develop segmental
47 overgrowth. How imbalanced PI3K signaling affects normal homeostasis to cause these very
48 different types of diseases is not understood because of a lack of information about its developmental
49 effects on interdependent organ systems in the context of mosaicism.

50 Tumor progression, increased microvascular density and cancer invasiveness are widely associated
51 with hyperactivity of PI3Ks and their downstream effectors. Normally, receptor tyrosine kinase-
52 mediated recruitment and activation of PI3Ks lead to appropriate production of second messengers
53 from lipid substrates. PI3Ks consist of a regulatory p85 subunit and one of three possible 110-kDa
54 catalytic subunits (p110α, p110β, p110δ). Mutations in *PIK3CA*, the gene encoding p110α, are alone
55 observed in 13% of all U.S. cancers (Mendiratta et al., 2021).

56 Once produced by an active PI3K, 3-phosphoinositide substrates can dock multiple possible
57 intracellular signal transducers, including the three AKT protein isoforms. Distinct combinations of
58 PI3Ks and AKTs seem to mediate a wide range of metabolic, trafficking, growth, survival,
59 proliferation and motility processes to coordinate cellular responses with other signaling pathways.
60 However, their specific effects have not been sufficiently characterized *in vivo* to understand how
61 their mutations lead to congenital disease.

62 The normal potential of neural crest (NC) stem cells to both influence and differentiate as a function
63 of surrounding tissues renders this population a prime target for growth factor receptor signaling
64 anomalies (Le Lievre and Le Douarin, 1975; Bergwerff et al., 1998; Etchevers et al., 1999, 2001;
65 Müller et al., 2008; Zachariah and Cyster, 2010). NC cells migrate away from the dorsal aspect of the
66 future brain and spinal cord towards the end of the first month of human gestation and engender a
67 wide variety of differentiated cell types (Le Douarin and Kalcheim, 1999). During their migration
68 throughout the embryonic head and body, they encounter many distinct and changing
69 microenvironments. Errors in the cross-talk between NC cells and their environment lead to a large
70 class of diseases collectively known as neurocristopathies (Bolande, 1974; Etchevers et al., 2019).

71 Craniofacial neurocristopathies are collectively frequent birth defects, including isolated or
72 syndromic cleft lip and/or palate (Juriloff and Harris, 2008) or the rarer craniosynostosis (Watt and
73 Trainor, 2014). After birth, NC-derived Schwann cell precursors in peripheral nerves remain a latent,
74 self-renewing multipotent stem cell pool that can be activated in response to multiple pathological
75 stimuli (Petersen and Adameyko, 2017; Xie et al., 2019). Given the multiple steps in NC
76 specification, migration and differentiation that are dependent on PI3K signaling (Ciarlo et al., 2017;
77 Sittewelle and Monsoro-Burq, 2018), we sought to discover the *in vivo* consequences of
78 constitutively active Pik3ca on the physiology of different populations of NC cells.

bioRxiv preprint doi: https://doi.org/10.1101/2022.04.05.487130; this version posted April 6, 2022. The copyright holder for this preprint (which was not certified by peer review) is the author/funder, who has granted bioRxiv a license to display the preprint in perpetuity. It is made available under aCC-BY-ND 4.0 International license.

3 Materials and Methods

3.1 Mouse lines

All mice were obtained directly or through Charles River France from the Jackson Laboratories (Bar Harbor, ME, USA) and intentionally outbred over multiple generations to CD-1/Swiss mice purchased from Janvier Laboratories in order to phenocopy human genetic heterogeneity. Knock-in lines included conditional, floxed *Pik3ca*^{H1047R} (RRID:IMSR_JAX:016977) (Adams et al., 2011) or *RdT*omato reporter mice (RRID:IMSR_JAX:007909); transgenics included the *Wnt1-Cre* (RRID:IMSR_JAX:003829), *Krox20-Cre* (RRID:IMSR_JAX:025744) and tamoxifen-inducible *Sox10-CreER*^{T2} (RRID:IMSR_JAX:027651) lines. 4-hydroxy-tamoxifen was solubilized in 10% ethanol, 90% corn oil and administered in a single intraperitoneal injection of 0.1 mL at 10 mg/mL. All mice were housed in individual, ventilated cages with 12-hr light/dark cycles with food and water *ad libitum*.

Mice were genotyped with 50 ng DNA purified from ear punch or tail clips using the primers described in the original reports and Phire Tissue Direct PCR Master Mix (Thermo Scientific).

3.2 Ethics approval

The animal study was reviewed and approved by the French national animal care and use committee (ACUC) C2EA-14 under the reference 9522-2017040517496865v5.

3.3 Histology, immunofluorescence and *in situ* hybridization

Embryos were staged taking embryonic day (E) 0.5 as the morning of the vaginal plug. Tissue biopsies were kept in ice-cold phosphate-buffered saline (PBS) until dissection, fixed in freshly thawed, neutral pH-buffered 4% paraformaldehyde for 20 minutes to overnight depending on tissue size, and rinsed again in PBS. Paraffin blocks were prepared according to standard embedding protocols, sections cut on a Leica microtome at 7 µm, and deparaffinated and rehydrated to PBS through xylene and decreasing ethanol solutions. Alternatively, fluorescent tissues were equilibrated in 15% then 30% sucrose in PBS and positioned in liquid embedding compound (Leica) before snap-freezing in plastic molds over liquid nitrogen. Cryosections were cut at 12 µM onto Superfrost Plus slides, dried, washed in PBS. All immunofluorescent sections were immersed for 20 minutes in 50 mM glycine, 0.1 M ammonium chloride before pre-incubating in a blocking solution of 0.1% Tween-20, 2% fetal calf serum in PBS and diluting the primary antibodies at the indicated concentrations for overnight treatment under Parafilm coverslips at 4°C. Standard procedures were followed for DAPI counterstain, subsequent Alexa Fluor-coupled secondary antibody (ThermoFisher) incubation and mounting with Fluoromount G (SouthernBiotech) under coverslips.

The following primary antibodies were used in this study: rat anti-Pecam1/CD31 (ThermoFisher, RRID:AB_467201), mouse anti-alpha-smooth muscle actin (Sigma-Aldrich, RRID:AB_10979529), rabbit anti-phosphorylated-S6 ribosomal protein (Ser235/236) (Cell Signaling Technologies, RRID:AB_2181035).

For the detection of *Pdgfra* transcripts on paraffin sections, we amplified a fragment as described by PCR (Orr-Urtreger et al., 1992) from cDNA prepared from a whole mouse embryo at E12.5. The reverse primer was prolonged by an additional T7 RNA polymerase recognition sequence (taatacgactcactatagggaga) added at the 5' end. *In vitro* probe synthesis, purification and a standard chromogenic *in situ* hybrization protocol were carried out as described (Thomas et al., 2018).

bioRxiv preprint doi: https://doi.org/10.1101/2022.04.05.487130; this version posted April 6, 2022. The copyright holder for this preprint (which was not certified by peer review) is the author/funder, who has granted bioRxiv a license to display the preprint in perpetuity. It is made available under aCC-BY-ND 4.0 International license.

120 Standard hematoxylin-eosin (HE; with or without Alcian blue to detect sulfated glycosaminoglycans)
121 staining protocols were followed for designated sections.

122 3.4 Microscopy

123 Gross anatomy was photographed with a Leica MZ6 dissecting microscope and images captured with
124 a DFC450 camera before analysis using the open-source ImageJ software (v1.53). Histology and *in*
125 *situ* hybridization slides were photographed on a Zeiss AxioScan 7 and immunofluorescent sections
126 on a Zeiss AxioZoom, Apotome or LSM800-Airyscan microscope equipped with Zen software (v2.3
127 or 3.0). Centroid size of crania was quantified in ImageJ by delimiting the shape above a virtual line
128 from the upper jaw to earlobe to occiput in the sagittal plane (Pilatti and Astúa, 2017).

129 3.5 Micro-X-ray computed tomography (µCT) examination

130 Late fetal (embryonic day [E]15.5-E20) specimens were genotyped and heads fixed overnight in 4%
131 buffered paraformaldehyde at 4°C. They were stored in PBS + 0.1% w/v sodium azide before
132 imaging on a X-ray micro-CT device (Quantum FX Caliper, Life Sciences, Perkin Elmer, Waltham,
133 MA) hosted by the PIV Platform, EA2496, Montrouge, France. The X-ray source was set at 90 kV
134 and 160 µA. Tridimensional images were acquired with an isotropic voxel size of 20 µm. Non-
135 mineralized tissues were visualized after impregnating with Lugol's solution.

136 Tiff image stills were extracted from Dicom data frames using licensed 64-bit Irfanview imaging
137 freeware (v4.59, http://www.irfanview.com/). Measurements were made in ImageJ after manual
138 segmentation using contrast thresholding.

139 4 Results

140 4.1 Constitutively active Pik3ca in most neural crest leads to perinatal death and craniofacial
141 malformations

142 In order to understand the effects of PI3K signaling in neural crest (NC) derivatives, we mated
143 conditional, floxed *Pik3ca*^{H1047R} and/or Tomato (*RdT*) reporter (Madisen et al., 2010) knock-in lines
144 with *Wnt1-Cre* transgenic mice, which express Cre recombinase in nearly all NC-derived cells from
145 pre-migratory stages onwards (Danielian et al., 1998). This engendered somatic mosaicism for
146 constitutive PI3K activation throughout the head and body of only those animals carrying both a
147 floxed *Pik3ca* and a *Cre* allele in those tissues expressing the recombinase.

148 No *Wnt1-Cre*; *Pik3ca*$^{H1047R/+}$ mice were recovered at weaning; in fact, all *Wnt1-Cre*; *Pik3ca*$^{H1047R/+}$
149 mice died within the first day after birth. The dead neonates did not present a belly milk spot and had
150 noticably large heads and cleft palates (**Figure 1**). In order to better understood the causes and onset
151 of death, we examined embryos at different stages of embryonic and fetal development up until birth.
152 Mutants were compared to their unaffected control littermates expressing only one or neither of the
153 *Wnt1-Cre* or *Pik3ca*$^{H1047R/+}$ alleles.

154 From E15.5 onwards, mutant crania were all visibly and significantly larger than controls (**Figure**
155 **1G, 2(A, E)**). Body sizes were unaltered. Macrocephaly was present both at the level of the cranial
156 vault and in the ossification of the mandible, which was significantly thicker in mutants (**Figure 2(B-**
157 **D** *vs.* **F-H)**). The phenotypic variability present within litters at birth was exacerbated in mutant
158 embryos, which all showed facial soft tissue asymmetry to degrees, and occasional premature
159 ossification along with overgrowth (**Figure (2H)** is a littermate of (**B-D**) and (**F-G**)).

bioRxiv preprint doi: https://doi.org/10.1101/2022.04.05.487130; this version posted April 6, 2022. The copyright holder for this preprint (which was not certified by peer review) is the author/funder, who has granted bioRxiv a license to display the preprint in perpetuity. It is made available under aCC-BY-ND 4.0 International license.

160 We sought additional causes of perinatal death because only approximately 50% of heads had
161 developed cleft secondary palates (**Figure 2(A)** *vs.* **2(E)**). Two possibilities were adrenal dysfunction
162 or cardiac malformation, both organs with vital neural crest-derived components for their
163 morphogenesis. We compared their sizes on soft tissue contrast-enhanced micro-CT sections of
164 E15.5-E16 embryos, as well as those of the pituitary, which controls adrenal function through the
165 function of its corticotroph cells, and the thymus, another neural crest-dependent gland (Müller et al.,
166 2008).

167 4.2 *Wnt1-Cre*; *Pik3ca*$^{H1047R/+}$ mice develop variable ocular and pituitary malformations

168 In contrast to the megalencephaly observed in mutants by E16, the anterior pituitary gland was
169 significantly smaller in micro-CT frontal sections of *Wnt1-Cre*; *Pik3ca*$^{H1047R/+}$ embryos than their
170 control littermates (**Figure 2(I-O)**). No significant differences were measured in maximal cross-
171 sectional areas of the adrenal glands or thymus (not shown). Variability in cardiac ventricular muscle
172 wall thickness was observed but on average, was not significantly different between mutant and
173 control embryos.

174 Initial cranial and trunk-level NC migration appeared to be unimpeded in *Wnt1-Cre*; *Pik3ca*$^{H1047R/+}$;
175 *RdT* mice versus their *Wnt1-Cre*; *RdT* littermates at E9.5 (**Figure 3(A-B)**). Likewise, at E13.5
176 (**Figure 3(C-H)**), palatal shelves, head size and the position of the tongue had not yet developed
177 obvious morphological differences. However, the eyes already appeared slightly malpositioned.
178 Since signaling through the Pdfgra receptor for platelet-derived growth factor is known to be crucial
179 for palatal development in both mice and humans (Tallquist and Soriano, 2003; Ding et al., 2004), we
180 undertook *in situ* hybridization to its transcript. The expression pattern of *Pdgfra* was unaltered in the
181 palatal NC-derived mesenchyme at E13.5, consistent with PI3K-mediated transduction being
182 downstream of Pdgfra in these cells (He and Soriano, 2013). Lens coloboma and microspherophakia,
183 an enlarged epithelial *Pdgfra* domain expression overlying a lack of primary fibers, and a thickened
184 cornea were already evident in mutants (**Figure 3(I-M)**).

185 4.3 PI3K signaling in NC-derived vascular smooth muscle induces venous malformations

186 One striking feature of *Wnt1-Cre*; *Pik3ca*$^{H1047R/+}$ mutants was the systematic presence of variable
187 degrees of craniofacial vascular malformations from E13.5 onwards (**Figure 4**). These most
188 resembled venous malformations in that they were low-flow, circumscribed congenital lesions within
189 the NC-derived dermis over the frontal bones and, frequently, in the maxillary and retroorbital
190 regions (**Figure 4 (A-D)**). The malformations often contained thromboses and were also observed in
191 the heart, in both ventricles and atria.

192 In order to examine the composition of these abnormal vascular structures, we examined the
193 distribution of the mural pericyte and smooth muscle marker, α-smooth muscle actin (aSMA) and the
194 endothelial marker Pecam-1 (CD31) in *Wnt1-Cre*; *Pik3ca*$^{H1047R/+}$ mutants using immunofluorescence
195 (**Figure 4 (E-F)**). Vascular smooth muscle of the cardiac great arteries, derived from posterior
196 rhombencephalic NC cells, was present but disorganized; the nuclei were not organized in their usual
197 concentric layers.

198 Within the intracardiac lesions, *Wnt1-Cre*; *Pik3ca*$^{H1047R/+}$; *RdT* mutants showed co-expression of the
199 Tomato NC lineage marker with aSMA in a discontinous manner around the vascular lacunae
200 (**Figure 4 (G), arrow**). Where aSMA was present, the cells were somewhat but not entirely
201 disorganized. They were somewhat cuboid rather than lamellar within the vascular media. A
202 cutaneous vascular malformation in the skin over the parietal bone in a late fetus at E20.5 (**Figure 4**

bioRxiv preprint doi: https://doi.org/10.1101/2022.04.05.487130; this version posted April 6, 2022. The copyright holder for this preprint (which was not certified by peer review) is the author/funder, who has granted bioRxiv a license to display the preprint in perpetuity. It is made available under aCC-BY-ND 4.0 International license.

203 **(H))** showed mutant aSMA-expressing, lineage-traced NC cells in dermal blood vessels surrounding
204 the hair follicles. This observation was remarkable since the NC-derived dermis, vascular pericytes,
205 meninges and craniofacial bones usually occupy the same territories of the ventral head and neck
206 (Etchevers et al., 1999). Given that the mouse parietal bone is of mesodermal rather than NC origin,
207 as shown by lineage tracing in a cross of the same *Wnt1-Cre* line with a conditional reporter allele
208 (Jiang et al., 2002), this implies that PI3K signaling may enable some NC derivatives to spread to
209 ectopic cranial regions before birth.

210 **4.4 PI3K signaling in muscle leads to widespread, progressive vascular anomalies**

211 Despite the striking and lethal phenotype of Pik3ca constitutive activity in mesectodermal cephalic
212 NC, we did not observe any changes in NC derivatives in the trunk in *Wnt1-Cre*; *Pik3ca*^{H1047R}
213 mutants at birth. This included the adrenal medulla and the enteric, autonomic or sensory nervous
214 systems. In order to examine a subset of cardiac NC in the developing tricuspid valves (Odelin et al.,
215 2018), we crossed the conditional, floxed *Pik3ca*^{H1047R} and/or Tomato (*RdT*) reporter knock-in lines
216 to the *Krox20-Cre* transgenic line, where Cre recombinase is expressed in the place of one allele of
217 the conserved zinc finger transcription factor Egr2 (Voiculescu et al., 2000).

218 Given the previously described expression of Krox20 in tendons, chondrocytes and osteocytes in
219 addition to a subpopulation of hindbrain NC cells and myelinating Schwann cells (Voiculescu et al.,
220 2000; Maro et al., 2004), we examined *Krox20-Cre*$^{+/\circ}$; *Pik3ca*$^{H1047R/+}$ mice for signs of cardiac
221 insufficiency from myxomatous valves, skeletal defects or peripheral neuropathy. *Krox20-Cre;*
222 *Pik3ca*$^{H1047R/+}$ were initially healthy and viable, but over time post-weaning developed palpable
223 lumps under the skin on the back, leg or tail and had soon reached a humane endpoint. Upon autopsy,
224 we discovered widespread, lobular vascular structures filled with coagulated blood in the
225 subcutaneous *panniculus carnosus* muscle, but also in and around skeletal, cardiac and smooth
226 muscles, the lungs, the reproductive organs and many other densely vascularized tissues (**Figure 5**
227 (**A-D, G-T**). These vascular lesions had cavernoma-like fibrous septa, and the adjacent nerves were
228 surrounded by loose fat. No phleboliths were observed and hearts appeared normal. Myelinated
229 sciatic nerves showed no macroscopic or functional differences between mutant and control mice.
230 However, mutant mice systematically developed splenomegaly (**Figure 5**(**E**, **F**)).

231 *Krox20-Cre*$^{+/\circ}$; *Pik3ca*$^{H1047R/+}$; *RdT*$^{+/\circ}$ mice, like their *Krox20-Cre*$^{+/\circ}$; *RdT*$^{+/\circ}$ counterparts, expressed
232 the fluorescent Tomato marker in the smooth muscle of the gonad (**Figure 5**(**H**)), in finely ramified
233 cells, probably reticular fibroblasts, in the spleen (**Figure 5**(**J**)), and in skeletal muscles throughout
234 the body. As expected, cells in the aorta and pulmonary trunk were derived from *Krox20*-expressing
235 progenitors (**Figure 5**(**L**)), but there were also scattered, filamentous cells throughout the walls of the
236 ventricles and to a lesser extent, the atria, corresponding to the sites of developing cardiac vascular
237 lesions in mutant animals (**Figure 5**(**D, I, M**)). A search for *Egr2* expression in a recent multi-organ
238 database of single adult mouse fibroblasts and vascular mural cells
239 (https://betsholtzlab.org/Publications/FibroblastMural/database.html) (Muhl et al., 2020)
240 demonstrated that the cells that had expressed *Krox20-Cre* were likely to be endomysial and
241 perimysial fibroblasts in cardiac and skeletal muscle, myelinating Schwann cells and endoneural
242 fibroblasts in the peripheral nerves, and a subtype of vascular pericytes, fibroblasts and smooth
243 muscle. Indeed, fascicles of the peripheral nerves, including autonomic, and a ring of probable
244 pericytes (Topilko, 2019) at the base of hair follicles in the non-glabrous skin strongly expressed RdT
245 in adulthood (**Figure 5**(**L**, **N**, **O**)), supporting the independent single-cell data and explaining the
246 widespread and unexpected vascular phenotypes in *Krox20-Cre*$^{+/\circ}$; *Pik3ca*$^{H1047R/+}$ mutant mice.

bioRxiv preprint doi: https://doi.org/10.1101/2022.04.05.487130; this version posted April 6, 2022. The copyright holder for this preprint (which was not certified by peer review) is the author/funder, who has granted bioRxiv a license to display the preprint in perpetuity. It is made available under aCC-BY-ND 4.0 International license.

247 ### 4.5 Egr2-driven *Pik3ca* $^{H1047R/+}$ expression induces postnatal pituitary and intramuscular
248 artery remodeling

249 Since *Krox20-Cre*$^{+/°}$; *Pik3ca*$^{H1047R/+}$ mice survived to adulthood, we made a cursory examination of
250 the pituitary gland for morphological or functional anomalies to compare to the *Wnt1-Cre*$^{+/°}$;
251 *Pik3ca*$^{H1047R/+}$ phenotype. Lineage tracing demonstrated that most if not all cells of the
252 adenohypophysis, unlike the neurohypophysis, had once expressed the Krox20 transcription factor
253 (**Figure 6**(**A**, **B**)). Examination of the capillary network in control mice with Pecam1 (CD31)
254 immunofluorescence in confocal microscopy showed that even endothelial cell nuclei showed
255 Tomato fluorescence (**Figure 6**(**C-F**)). Intriguingly, mutant pituitaries had many nuclei of cells that
256 had replaced those descended from progenitors that had once expressed Krox20 but were not RdT+.
257 There were fewer RdT+ cells overall and this was accompanied by a concomitant decrease in
258 Pecam1+/ RdT+ cell density (**Figure 6**(**G-J**)) but not in organ size or, apparently, function.

259 A recent report has implicated increased PI3K signaling in the formation of cerebral cavernous
260 malformations (CCMs) and phosphorylated S6 (p-S6) ribosomal protein expression as its endothelial
261 intermediary (Ren et al., 2021). We therefore sought, but did not observe, similarly increased
262 expression of p-S6 in the vascular lesions of the *Krox20-Cre*$^{+/°}$; *Pik3ca*$^{H1047R/+}$ mice (**Figure 6**(**O**, **S**)).
263 Slightly increased expression was sometimes observed in the abnormally shaped vascular smooth
264 muscle cells of muscular cavernomas, co-expressing alpha-smooth muscle actin (**Figure 6**(**M**, **O,**
265 arrows)), but not in the thickened, disorganized smooth muscle walls of the coronary artery (**Figure**
266 **6**(**Q**, **S**)).

267 ### 4.6 Melanocytic and other tumors

268 In many *Krox20-Cre*$^{+/°}$; *Pik3ca*$^{H1047R/+}$ mutants, vascular anomalies were accompanied by
269 widespread, extracutaneous pigmented melanocyte deposits (**Figure 7**(**A**)). In the meninges of the
270 head, although some melanocytosis is physiological in mice (Gudjohnsen et al., 2015), the olfactory
271 lobes (**Figure 7**(**B**)) and trigeminal nerves were covered in a melanocytic mesh. Pigmented
272 melanocytes were also conspicuous in the capillary network of the lower incisor gingiva (**Figure**
273 **7**(**C**)), which has not been described to our knowledge as a site for extracutaneous melanocytes.
274 Some adults developed melanocytic tumors in addition to their vascular anomalies (**Figure 7**(**D**)).
275 These regularly invested distant lymph nodes and were found in multiple sites, but without the
276 typical tropism for brain, liver or lung, where tumors were never observed. Such mice rapidly
277 reached humane endpoints. A rhabdomyomatous mesenchymal hamartoma was also observed in the
278 inner thigh of one mutant mouse (**Figure 7**(**E**)).

279 We hypothesized that peripheral Schwann cells could be a source of such widely distributed
280 extracutaneous melanocytes and that the expression of constitutively active Pik3ca therein would
281 favor their phenotypic switch. To test this *in vivo*, *Sox10-CreER*^{T2} mice were crossed with floxed
282 *Pik3ca*$^{fl(H1047R)/+}$ mice to produce a tamoxifen-inducible Cre recombinase in *Sox10*-expressing cells.
283 At adult stages, these include but are not restricted to nerve-resident peripheral glia and their
284 precursors (Deal et al., 2021). Four female *Sox10-CreER*^{T2}; *Pik3ca*$^{H1047R/+}$ from two litters were
285 injected with 1 mg 40H-TAM at 15-19 weeks and compared to four similarly treated *Sox10-CreER*^{T2};
286 *RdT* mice (three female, one male) and one female *Pik3ca*$^{fl(H1047R)/+}$ controls of the same age. Within
287 five days, one mutant had died and the three others had attained a humane endpoint and were
288 euthanized. Cause of death was not determined, but gross examination of the *Sox10-CreER*^{T2}; *RdT*
289 mice under a fluorescence binocular dissecting microscope demonstrated effective recombination had
290 been induced in all. Although no obvious tumors had developed in the mutants, the superficially

bioRxiv preprint doi: https://doi.org/10.1101/2022.04.05.487130; this version posted April 6, 2022. The copyright holder for this preprint (which was not certified by peer review) is the author/funder, who has granted bioRxiv a license to display the preprint in perpetuity. It is made available under aCC-BY-ND 4.0 International license.

291 pigmented axillary and Peyer's patch lymph nodes had enlarged germinal centers (not shown), and
292 the ovaries were lumpy (**Figure 7**(**F**)).

293 *Sox10-CreER*^{T2} males were then mated to three *Pik3ca*$^{\text{flox(1047R)/+}}$ females and the pregnant dams
294 treated at E18.5 with 4OH-TAM to induce recombination in post-migratory NC and other Sox10-
295 expressing cells just before birth. This led to recovery of a total of ten live births: five *Sox10-*
296 *CreER*^{T2}; *Pik3ca*$^{\text{H1047R/+}}$ (three female, two male), four *Sox10-CreER*^{T2} and one male *Pik3ca*$^{\text{H1047R/+}}$
297 mouse. These animals were followed without incident for up to 1 year, when one male mutant rapidly
298 developed an unpigmented, circumscribed tail tumor of 5 mm in diameter and showed signs of
299 distress. After euthanasia, the tumor could be seen to contain varied cellular elements including
300 smooth muscle and mucin-containing myxoid zones that stained with Alcian blue (**Figure 7**(**G**)). Our
301 observations support other recent studies that highlight the importance of positional and lineage
302 context for the carcinogenic potential of oncogenic mutations (Baggiolini et al., 2021) and imply that
303 it may extend beyond MAP kinases to the PI3K signaling pathway.

304 # 5 Discussion

305 ## 5.1 Vascular tumor-like malformations arise from impaired endothelial-mural interactions

306 *PIK3CA* gain-of-function mutations have been shown to lead to constitutive activation of Akt
307 downstream of the TEK angiopoietin-1 receptor in human vascular endothelial cells (Limaye et al.,
308 2015) as well as in targeted mouse models (Castillo et al., 2016), where TEK is known as Tie2.
309 Nearly half of sporadic venous malformations (VMs) bear activating *TEK* mutations while others
310 express activating *PIK3CA* H1047R, or E452K or C420R mutations, in a mutually exclusive manner
311 (Castel et al., 2016). These, particularly H1047R, are the most frequent hotspot mutations for breast
312 and colon cancer, but also malignancies in 45 other tissues and over 21,000 samples curated by
313 COSMIC (v95) to date (Stone, 1926; Le Lièvre, 1978; Etchevers et al., 2019).

314 The work we present here is the first to demonstrate that activation of the same signaling pathway by
315 the same mutation in adjacent perivascular pericytes and vascular smooth muscle also can induce
316 congenital vascular malformations. It has long been understood that paracrine signaling between
317 adluminal and abluminal cells is necessary for tissue-appropriate, functional blood and lymphatic
318 vessel assembly. Pharmacological PI3K inhibition rescues inducible arteriovenous malformations in
319 the context of an inducible animal model for a recurrent transforming growth factor-b (TGF-b)/bone
320 morphogenetic protein (BMP) signalling pathway gene mutation known to cause hereditary
321 hemorrhagic telangiecstasia (Ola et al., 2016). Recent models for CCMs also feature upregulated
322 PI3K activity and increased p-S6 in endothelial cells, unlike what we have initially observed in the
323 vascular lesions induced before or after birth by increased PI3K signaling in mural cell progenitors
324 with immunofluorescence. However, activation of pAkt, p-S6 and other pathway effectors in the
325 connective tissues of patients with PIK3CA-mutated fibroadipose vascular anomalies (FAVA)
326 indicate that the syndromic aspects are not dissociable from the vascular tumor-like malformations
327 themselves (Hori et al., 2020). Further functional work will be needed to define the additional
328 mediators and intracellular effectors of endothelial-mural paracrine exchanges in these new models

329 NC cells are a minority but crucial lineage in cardiac function and development . As contributors to
330 melanocytic, glial, parasympathetic neuronal and a small fraction of pericytic and cardiomyocyte
331 lineages, their role is essentially paracrine. The fact that both *Wnt1-Cre*; *Pik3ca*$^{\text{H1047R/+}}$ and *Krox20-*
332 *Cre*; *Pik3ca*$^{\text{H1047R/+}}$ mice present vascular anomalies within cardiac tissue implies that PI3K signaling
333 to a cell of NC origin in the heart has an impact on its subsequent secretory activity, with a similar
334 effect on intracardiac vascular development as in the head and neck. In the future, single-nucleus

bioRxiv preprint doi: https://doi.org/10.1101/2022.04.05.487130; this version posted April 6, 2022. The copyright holder for this preprint (which was not certified by peer review) is the author/funder, who has granted bioRxiv a license to display the preprint in perpetuity. It is made available under aCC-BY-ND 4.0 International license.

335 RNA sequencing of both cardiac ventricles and craniofacial mesenchyme could be an approach to
336 identify such vasculogenic factors secreted by lineage-traced cardiac pericytes and glia in these
337 mouse crosses.

338 5.2 PI3K activity in NC cells also induces megalencephaly, jaw hyperplasia and cleft palate

339 In contrast to blood and lymphatic vessels, where the endothelium is always of mesodermal origin,
340 the constitutive activation of Pik3ca in cells having expressed Wnt1 in the neuroepithelium before
341 neural crest migration also led to apparently autonomous effects in the brain, while only some
342 mesectodermal NC derivatives were affected (Le Lievre and Le Douarin, 1975). Lineage tracing with
343 a floxed Rosa-tomato fluorescent reporter allele did not show any differences in NC distribution after
344 migration into the face and head at E9.5, implicating PI3K signaling in the later differentiation of
345 cephalic NC-derived mesenchyme into perivascular cells and other connective tissues, a potential
346 outcome not available to truncal NC progeny in mammals (Etchevers et al., 2001; Deal et al., 2021).
347 This may explain why there were no apparent effects at the level of the trunk in neonates, although
348 we may have missed subtle effects on vagal innervation of the heart or gut.

349 Cranial NC mesenchyme and nerves normally secrete vascular endothelial growth factor (VEGF) to
350 promote mandibular artery extension, stabilization through mural coverage and, thereby, support jaw
351 elongation (Wiszniak et al., 2015). Interfering with signaling to the endothelial VEGF receptor, Nrp1,
352 phenocopies mandibular artery loss and hemifacial microsomia in human patients.

353 We have seen in gross dissection and micro-CT that when cranial NC expresses constitutively active
354 Pik3ca, there is the opposite phenotype: vascular and jaw hyperplasia. A clear association between
355 vascular and craniofacial overgrowth has been reported clinically for decades, well before human
356 genetics caught up (Krings et al., 2007). Facial capillary malformations found in Sturge-Weber
357 syndrome are usually due to constitutively activating, somatic *GNAQ* mutations (Shirley et al., 2013)
358 but are regularly associated with segmental overgrowth of the orbit or the jaw and in at least one
359 report, additional somatic mutations, including one in *PIK3CA* (Lian et al., 2014). This missense
360 mutation has been reported 134 times to date in COSMIC (https://cancer.sanger.ac.uk/cosmic) with a
361 high pathogenicity score (0.97). G-protein and PI3K signaling cascades are both likely to mediate the
362 exchanges of vascular cross-talk with NC-derived mesenchyme and the subsequent skull growth
363 anomalies that can extend throughout life.

364 5.3 Congenital overgrowth usually does not lead to malignancy but presents its own problems

365 Somatic mutation of codon H1047 is frequently but not exclusively implicated in asymmetric, multi-
366 systemic *PIK3CA*-related overgrowth disorders such as CLOVES [OMIM 612918; congenital
367 lipomatous overgrowth, vascular malformations, epidermal nevi and skeletal abnormalities] and
368 endophenotypic segmental overgrowth syndromes affecting muscle and fat, or fibroadipose
369 hyperplasia. Another class of PRDs involve megalencephaly with various other features affecting
370 musculoskeletal, vascular, connective and adipose tissues, of which megalencephaly-capillary
371 malformation-polymicrogyria syndrome (MCAP) is emblematic (Lee et al., 2012; Kingsmore et al.,
372 2013; Alcantara et al., 2017). PI3K inhibitors have been very promising in clinical trials for these
373 conditions (eg. Dill et al., 2014; Roy et al., 2015; Venot et al., 2018; Hori et al., 2020)

374 Some patients develop supernumerary, hypertrophic muscles in the upper limbs; these are
375 occasionally bilateral, indicating that the original somatic mutation may have developed in a cell
376 whose progeny entered the paraxial mesoderm cell during gastrulation (Frisk et al., 2019). While
377 nearly half of overgrowth PRD patients in one cohort presented vascular malformations, the

bioRxiv preprint doi: https://doi.org/10.1101/2022.04.05.487130; this version posted April 6, 2022. The copyright holder for this preprint (which was not certified by peer review) is the author/funder, who has granted bioRxiv a license to display the preprint in perpetuity. It is made available under aCC-BY-ND 4.0 International license.

378 congenital tissue overgrowth in the vast majority continued to evolve postnatally (Keppler-Noreuil et
379 al., 2014). Malignant tumors in PRD patients are nonetheless surprisingly rare, given that they
380 express proven oncogenic mutations, and this finding was borne out in our mouse models. However,
381 the resultant malformations themselves were not always compatible with viability.

382 We have observed that benign vascular and/or hamartoma-like tumors can arise postnatally in mice
383 expressing constitutively active Pik3ca in a mosaic fashion, in cells having expressed the
384 *Krox20*/*Egr2* or *Sox10* transcription factors. Both of these transcription factors are hallmarks of so-
385 called "Schwann cell precursors" or SCP. SCP are NC-derived, non-myelinating cells that reside
386 along or at the terminal ends of peripheral nerves, and that can respond to environmental changes
387 such as injury or inflammation by differentiating into myelinating Schwann cells and endoneurial
388 fibroblasts but also melanocytes in rodents (Adameyko et al., 2009). Interestingly, these resident,
389 poised cells also normally contribute extracutaneous melanocytes to the heart, inner ear, ocular
390 choroid plexus, to some normal skeletal muscles such as the quadriceps (evident in the gastrocnemius
391 of pigmented mice, unpublished observations) and the CNS meninges (Kaucka et al., 2021).

392 Some melanocytosis was seen in the hypothalamic meninges and membranes surrounding the
393 trigeminal nerves of adult pigmented *Krox20-Cre;RdT* mice without additional Pik3ca activity.
394 However, in agouti or black tamoxifen-induced *Sox10-CreER*^{T2} control mice, it did not appear to
395 increase in extent from normal meningeal pigmentation (Gudjohnsen et al., 2015). This implies that
396 dosage reduction of Egr2 may be a prerequisite to SCP plasticity and would be a testable hypothesis
397 for the future. Our findings show that these partially committed progenitors at any stage of life are
398 particularly vulnerable to the effects of constitutively active PI3K signaling.

399 **5.4 Pik3ca-related disorders may encompass previously unsuspected pathologies**

400 The wide variety and range in severity of PRD phenotypes is attributed in part to the location of the
401 cells bearing the mutation and to the proportion of cells affected in each of any given patient's
402 tissues. We identified effects of constitutive PI3K signaling on pituitary and palatal development that
403 are not features of the diverse PRDs already identified to date.

404 Adrenal insufficiency could contribute to perinatal mortality in our *Wnt1-Cre*; *Pik3ca*$^{H1047R/+}$ mice,
405 since when constitutive Akt signaling is induced in the embryonic ectoderm, crucial proteins for
406 differentiation of the corticotroph lineage, such as Bmp4 and Tbx19, are significantly down-regulated
407 in mice (Segrelles et al., 2008). If so, this would be another measure of paracrine NC effects on
408 pituitary development Interestingly, the fact that *Krox20-Cre*; *Pik3ca*$^{H1047R/+}$ survived to adulthood
409 despite constant PI3K activity in all anterior pituitary cells would imply that it is the action of Pik3ca
410 signaling in resident NC-derived cells in the pituitary or its meninges that led to the hypoplasia we
411 regularly observed by birth. Such hypotheses and the nature of this paracrine activity exerted by NC-
412 derived cells could be further investigated in these mouse models.

413 Lineage-traced *Krox20-Cre; RdT* mice showed a much broader distribution of cells in the body that
414 had once or continued to express *Egr2* than previously described. Evidence exists that some of these
415 are cutaneous vascular pericytes derived from Schwann cell precursors, themselves from a NC-
416 derived "boundary cap cell" population residing adjacent to the spinal cord (Gresset et al., 2015;
417 Topilko, 2019). However, many also appear to be specialized fibroblasts primed by this transcription
418 factor (Muhl et al., 2020).

419 The sites of predilection for *Krox20-Cre*; *Pik3ca*$^{H1047R/+}$ vascular lesions were within the *panniculus*
420 *carnosus* and epaxial skeletal muscle groups, compatible with intramuscular hemangioma, a tumor

bioRxiv preprint doi: https://doi.org/10.1101/2022.04.05.487130; this version posted April 6, 2022. The copyright holder for this preprint (which was not certified by peer review) is the author/funder, who has granted bioRxiv a license to display the preprint in perpetuity. It is made available under aCC-BY-ND 4.0 International license.

421 rather than a vascular malformation (Tan et al., 2007; Kurek et al., 2012). Unlike soft-tissue
422 angiomatosis, we did not observe a mature adipose or lipomatosis component to these lesions, or
423 indeed in any of the other described mouse models. However, adipocytes do collect around
424 peripheral nerves (**Figure 5(A-B)**) in our *Krox20-Cre*; *Pik3ca*$^{H1047R/+}$ mice. This observation may be
425 relevant for the study of fibrolipomatous hamartoma, which like other PRDs is often associated with
426 overgrowth of the innervated territory (Marek et al., 2021). Somatic or germline mutations in *PTEN*,
427 leading indirectly to PI3K pathway activation, also predispose to cancer, localized tissue overgrowth
428 and are frequently associated with intramuscular vascular anomalies (Tan et al., 2007; Ho et al.,
429 2012).

430 Recently, gain-of-function *Pik3ca* mutations have been demonstrated to be sufficient to drive small,
431 postnatal capillary hemangiomas in brain endothelial cells and are necessary, in combination with
432 mutations of known CCM genes in mice or in humans, for the development of large postnatal
433 cavernomas (Hong et al., 2021; Ren et al., 2021). Should *PIK3CA* mutations also be confirmed in
434 human intramuscular hemangiomas or fibrolipomatous hamartomas, they would be the functional
435 and tumoral counterpart of soft-tissue hamartomas due to *PTEN* mutations (Kurek et al., 2012; Luks
436 et al., 2015; Tachibana et al., 2018). In these congenital and predisposing conditions, evolving
437 anomalies are not always surgically accessible and can be aggravated in the case of incomplete
438 resection. Targeted inhibitors of distinct pathway levels, potentially locally infused and in
439 combination, show great promise and can now be tested in a wider range of tailored animal models.

440 # 6 Figure legends

441 **Figure 1**. Mutants compared to their unaffected control littermates expressing only one or neither of
442 the *Wnt1-Cre* or *Pik3ca*$^{H1047R/+}$ alleles.

443 (**A**) At E20.5, fetal head from control littermate of (**B**) at same magnification, facing left.
444 (**B**) At E20.5, mutant fetus like newborns had visible megalencephaly, displaced eyes above an
445 enlarged maxillary primordium and skull vault, larger external ears, a longer nose, and facial vascular
446 malformations (arrowheads). Bar, 1 mm.
447 (**C**) Same fetus as in (**A**), skin removed and relative interocular distance indicated in square bracket.
448 Bar, 2 mm.
449 (**D**) Same fetus as in (**B**), skin removed to see hemorrhage from ruptured vascular malformations.
450 Bar, 2 mm.
451 (**E**) *Wnt1-Cre*$^{+/°}$;*Pik3ca*$^{H1047R/+}$ mutant newborn at P0, view of cleft palate (bracket) after removal of
452 skin and jaw. Bar, 2 mm.
453 (**F**) *Wnt1-Cre*$^{+/°}$;*Pik3ca*$^{H1047R/+}$ mutant newborn at P0, coronal view of cleft palate (bracket) after
454 removal of skin and jaw, relative interocular distance indicated in square bracket at same scale as
455 (**C**). Arrowhead, vascular malformation. Bar, 2 mm.
456 (**G**) Maximum sagittal plane surface projection of lateral photographs from embryos at the indicated
457 stages between embryonic day (E)15 and birth (P0), of either control (ctrl) littermate or *Wnt1-Cre*$^{+/°}$;
458 *Pik3ca*$^{H1047R/+}$ (mut) genotype. Through the last third of gestation, mutant heads were significantly
459 larger than controls, as was the head of the sole neonate recovered.
460 e, eye
461
462 **Figure 2**. Micro-computed tomography (micro-CT) of skull development in *Wnt1-Cre*$^{+/°}$;
463 *Pik3ca*$^{H1047R/+}$ mice at late fetal stages.
464 (A) Control littermate fetus at E15.5 in (E) – representative micro-CT frontal section through eyes,
465 brain, palate, tongue and jaw.

bioRxiv preprint doi: https://doi.org/10.1101/2022.04.05.487130; this version posted April 6, 2022. The copyright holder for this preprint (which was not certified by peer review) is the author/funder, who has granted bioRxiv a license to display the preprint in perpetuity. It is made available under aCC-BY-ND 4.0 International license.

466 (B, C, D) 3D projections in frontal view of the mineralization of three representative skulls of control
467 littermate fetuses at E20.5 in (B-D). The arrow indicates mandibular bone thickness.
468 (E) Control littermate embryo of of E15.5 embryo in (A) – representative micro-CT frontal section
469 through eyes, brain, cleft palate, malpositioned tongue (arrow) and jaw.
470 (F, G, H) 3D projections in frontal view of the mineralization of three representative skulls of control
471 littermate fetuses at E20.5 in (F-H). The arrow indicates mandibular bone thickness.
472 (I, J, K) Representative micro-CT frontal sections through the pituitary gland (boxed) in three control
473 fetuses at E15.5.
474 (L, M, N) Representative micro-CT frontal sections through the pituitary gland (boxed) in three
475 *Wnt1-Cre*$^{+/\circ}$; *Pik3ca*$^{H1047R/+}$ fetuses at E15.5. The morphology of the pituitary in N appears normal,
476 unlike in L and M.
477 (O) Segmentation analysis of the largest surface areas of the pituitary in the same sectional plane,
478 shows a significant reduction in pituitary size at 15-16 embryonic days ($p>0.01$, $n=6$ controls versus
479 6 mutants).
480 a.u., arbitrary units; ctrl, control; mut, mutant.
481
482 **Figure 3.** Phenotypes of *Wnt1-Cre*$^{+/\circ}$; *Pik3ca*$^{H1047R/+}$ embryos from E9.5 to E13.5.
483 (A) When lineage-traced by co-expression of a *RdT*$^{+/\circ}$ allele to transcribe Tomato red fluorescent
484 protein in cells having expressed Wnt1, *Wnt1-Cre*$^{+/\circ}$; *RdT*$^{+/\circ}$ embryos at E9.5 show the normal
485 distribution of neural crest (NC) mesenchyme in the face and pharyngeal arches. Bars = 0.5 mm for
486 A, B.
487 (B) *Wnt1-Cre*$^{+/\circ}$; *Pik3ca*$^{H1047R/+}$; *RdT*$^{+/\circ}$ embryos at E9.5 show unaltered distribution of NC-derived
488 mesenchyme in the pharyngeal arches, frontonasal bud or body.
489 (C) Left side of E13.5 control littermate to (D). Lack of pigment in retinal pigmented epithelium of
490 eye is normal for a mouse that would have been born albino (Tyr^{c}/ Tyr^{c}), a background allele
491 (http://www.informatics.jax.org/allele/MGI:1855976). Bars = 2 mm for C, D.
492 (D) Left side of E13.5 *Wnt1-Cre*$^{+/\circ}$; *Pik3ca*$^{H1047R/+}$ littermate to C, showing vascular anomalies and
493 cerebral hemorrhage.
494 (E) Paraffin parasagittal section of control littermate head of (F) at E13.5, stained with HE. Bars =
495 0.5 mm for E, F, G, H, L, M.
496 (F) Paraffin sagittal section of mutant head at E13.5 showing enlarged frontonasal and mandibular
497 tissues, cerebellar isthmus and choroid plexus, as well as a malpositioned Rathke's pouch relative to
498 the infundibulum, stained with HE.
499 (G) Paraffin frontal section of control head at E13.5 showing physiological position of tongue
500 between palatal shelves and converging maxillary processes, stained with HE.
501 (H) Paraffin frontal section of mutant littermate of (G) at E13.5, showing lens coloboma, thickened
502 corneal epithelium and less convergent maxillary proceeses than in (G), stained with HE.
503 (I) *In situ* hybridization with a Pdgfra probe in a control embryo at E13.5 shows transcript expression
504 in blue in craniofacial mesenchyme around the ocular primordium, particularly in the lens epithelium
505 and corneal stroma, but not in the lenticular primary fibers. Bars I, J, K = 0.2 mm.
506 (J) Mutant embryos express *Pdgfra* normally within the ocular primordium at E13.5, but have
507 microphakia.
508 (K) An adjacent section to (J) shows an enlarged, *Pdgfra*+ hyaloid vasculature relative to the control
509 embryo section in (I).
510 (L) A control frontal section at E13.5 after *Pdfra in situ* hybridization.
511 (M) A mutant frontal section of an embryo at E13.5 after *Pdfra in situ* hybridization. Palatal, digital
512 or mesenchymal expression are not qualitatively different.
513

bioRxiv preprint doi: https://doi.org/10.1101/2022.04.05.487130; this version posted April 6, 2022. The copyright holder for this preprint (which was not certified by peer review) is the author/funder, who has granted bioRxiv a license to display the preprint in perpetuity. It is made available under aCC-BY-ND 4.0 International license.

514 **Figure 4**. Vascular lesions are present before birth with disorganized mural elements in *Wnt1-Cre*;
515 *Pik3ca*$^{H1047R/+}$ mutants.
516 (**A**) Mutant embryo at E15.5 with periocular vascular anomalies.
517 (**B**) Mutant littermate of (A) with segmental vascular anomalies in the maxillary region.
518 (**C**, **D**) Mutant E20 fetuses. (**C**) was dead *in utero* and had a vascular lesion on the mandible. Both
519 showed maxillary and posterior periocular vascular anomalies and megalencephaly. Scale bars A-D,
520 2 mm.
521 (**E**) Control littermate and (**F**) mutant pulmonary trunk at E14.5; merged immunofluorescence (**E'**,
522 **F'**): yellow, endothelial marker Pecam-1 (CD31); (**E'', F''**) purple, smooth muscle marker, α-smooth
523 muscle actin (aSMA); (**E''', F'''**) blue, nuclear marker DAPI. Bars E, F = 50 µm.
524 (**G**) Cellular organization around an intracardiac vascular anomaly, showing a discontinuous (arrow)
525 smooth muscle layer of mutant NC origin.
526 (**H**) Facial skin of E20.5 mutant fetus (not the ones in C, D) with numerous double-labeled, small
527 capillary anomalies in upper dermis (arrow) around hair follicles.
528 (**G', H'**): Tomato fluorescent protein; (**G'', H''**): smooth muscle marker, α-smooth muscle actin
529 (aSMA); (**G''', H'''**) nuclear marker DAPI in blue. Bars G, H = 50 µm.
530

531 **Figure 5**. Anatomy and histology of vascular anomalies in *Krox20-Cre*$^{+/\circ}$; *Pik3ca*$^{H1047R/+}$ adult
532 mutant mice.
533 (**A**) Subcutaneous vascular anomaly, epaxial (*longissimus dorsi*) muscle. Bars A-I: 2 mm.
534 (**B**) Subcutaneous vascular anomaly, quadriceps.
535 (**C**) Vascular anomalies around left gonad.
536 (**D**) Mutant heart, small vascular anomaly at apex (arrow).
537 (**E**) Control littermate spleens of those in (F).
538 (**F**) Mutant spleens, same scale as (E).
539 (**G, H**) Vascular tumor around gonad from different mouse than in (C), *Krox20-Cre*$^{+/\circ}$;
540 *Pik3ca*$^{H1047R/+}$; *RdT*$^{+/\circ}$. The fluorescent fibroblasts in gonad and lesional septa had expressed Krox20
541 and thereby, constitutively active Pik3ca.
542 (**I**) Intracardiac vascular anomalies were present in all mutant adults examined.
543 (**J**) *Krox20-Cre*$^{+/\circ}$; *Pik3ca*$^{H1047R/+}$; *RdT*$^{+/\circ}$ spleens as in (**F**) had numerous fluorescent ramifications
544 consistent with reticular fibers, peripheral nervous or perivascular elements. Bar, 200 µm.
545 (**K**) Mutant femoral bone marrow in an adult mouse that had spontaneously died with multiple
546 vascular anomalies was hypocellular with increased density of vascular sinuses rather than adiposity.
547 Bar, 200 µm.
548 (**L**) Heart from a *Krox20-Cre*$^{+/\circ}$; *Pik3ca*$^{H1047R/+}$; *RdT*$^{+/\circ}$ mouse showing recombined cells in a fine
549 meshwork throughout the myocardium of all chambers with increased density in the ventral
550 pulmonary trunk and strong expression in the outer wall of a sympathetic nerve (arrow). Bar, 200
551 µm.
552 (**M**) Typical histology of vascular lacunae in the ventricular wall. Bar, 200 µm.
553 (**N**, **O**) Subcutaneous vascular tumor of tail. Bar, 2 mm.
554 (**P**) Dorsal aspect of lineage-traced mutant hairy skin. Fluorescence is visible at the base of each hair
555 follicle and in the vascular pericytes of capillaries underlying them. Bar, 200 µm.
556 (**Q**) Ventral aspect of lineage-traced mutant hairy skin. The *panniculus carnosus* muscle had
557 expressed *Krox20* (striations) and the peripheral nerves express *Krox20Cre*-driven Tomato even
558 more strongly in their myelinating Schwann cells. Bar, 0.5 mm.
559 (**R**) Vascular lacunae separate disrupt the organization of muscle bundles and their external
560 connective tissues in a mutant thigh. Bar, 200 µm.
561 (**S**) Disrupted vascular structures were also present in the mutant salivary gland.

bioRxiv preprint doi: https://doi.org/10.1101/2022.04.05.487130; this version posted April 6, 2022. The copyright holder for this preprint (which was not certified by peer review) is the author/funder, who has granted bioRxiv a license to display the preprint in perpetuity. It is made available under aCC-BY-ND 4.0 International license.

562 (**T**) A profusion of small vascular sinuses were enlarged and necrosis was visible in the mutant liver.
563 Bar = 100 μm.
564 ao, aorta; la, left atrium; lv, left ventricle; pt, pulmonary trunk; ra, right atrium; rca, right coronary
565 artery; rv, right ventricle, sa, septal artery.
566
567 **Figure 6**. Lineage tracing and immunofluorescence in *Krox20-Cre*$^{+/\circ}$; *Pik3ca*$^{H1047R/+}$ adult mutant
568 mice.
569 (**A**) Dorsal view of control pituitary after removal of brain and meninges.
570 (**B**) Dorsal view of *Krox20-Cre*$^{+/\circ}$; *RdT*$^{+/\circ}$ pituitary during dissection after removal of brain, showing
571 highly fluorescent adenohypophysis under visible light. Bar, 1 mm.
572 (**C-F**) Section through adenohypophysis of *Krox20-Cre*$^{+/\circ}$; *RdT*$^{+/\circ}$ mouse, showing normal cell
573 density and that most or all cell types, including perivascular nuclei, had expressed *Krox20*, unlike
574 the sparse recombination observed in the neurohypophysis (not shown). (**C**) Merged (**D**) Tomato (**E**)
575 Pecam1 (CD31) (**F**) DAPI fluorescence. Bar, 20 μm.
576 (**G-J**) Section through adenohypophysis of *Krox20-Cre*$^{+/\circ}$; *Pik3ca*$^{H1047R/+}$; *RdT*$^{+/\circ}$ mouse, showing
577 slightly reduced cell density but a striking reduction in cells that had expressed *Krox20*, implying
578 later compensation by endothelial and pituitary stem cells. Bar, 20 μm.
579 (**K, L**) Expression of alpha-smooth muscle actin (aSMA, orange) around vascular tumors (**K**) and in
580 a coronary artery and surrounding telangiecstatias (**L**). Area magnified in (**Q**) indicated.
581 (**M-P**) Mural structure in representative vascular anomaly. Slight increase of phosphorylated S6
582 kinase (**O**, purple, arrowheads) in a few among the disorganized and unusually shaped cells of the
583 aSMA-expressing vascular wall (**N**, orange). (**M**) Merged. (**P**) DAPI. Bar = 10 μm.
584 (**Q-T**) Mural structure of the coronary artery in (L). No apparent increase of phosphorylated S6
585 kinase (**S**, purple) but presence of disorganized and unusually shaped cells in the aSMA-expressing
586 vascular wall (**R**, orange), although some laminar structure is still present. (**Q**) Merged. (**T**) DAPI.
587 Bar = 10 μm.
588
589 **Figure 7**. Widespread melanocytic anomalies in conjunction with Krox20- or Sox10-driven
590 expression of constitutively active Pik3ca.

591 vascular anomalies were accompanied by widespread, extracutaneous pigmented melanocyte
592 deposits (**Figure 7**(**A**)). In the meninges of the head, although some melanocytosis is physiological in
593 mice (Gudjohnsen et al., 2015), the olfactory lobes (**Figure 7**(**B**)) and trigeminal nerves were covered
594 in a melanocytic mesh. Pigmented melanocytes were also conspicuous in the capillary network of the
595 lower incisor gingiva (**Figure 7**(**C**)), which has not been described to our knowledge as a site for
596 extracutaneous melanocytes. Some adults developed melanocytic tumors in addition to their vascular
597 anomalies (**Figure 7**(**D**)). These regularly invested distant lymph nodes and were found in multiple
598 sites, but without the typical tropism for brain, liver or lung, where tumors were never observed.
599 Such mice rapidly reached humane endpoints. A rhabdomyomatous mesenchymal hamartoma was
600 also observed in the inner thigh of one mutant mouse (**Figure 7**(**E**)).

601 We hypothesized that peripheral Schwann cells could be a source of such widely distributed
602 extracutaneous melanocytes and that the expression of constitutively active Pik3ca therein would
603 favor their phenotypic switch. To test this *in vivo*, *Sox10-CreER*^{T2} mice were crossed with floxed
604 *Pik3ca*$^{fl(H1047R)/+}$ mice to produce a tamoxifen-inducible Cre recombinase in *Sox10*-expressing cells.
605 At adult stages, these include but are not restricted to nerve-resident peripheral glia and their
606 precursors (Deal et al., 2021). Four female *Sox10-CreER*^{T2}; *Pik3ca*$^{H1047R/+}$ from two litters were
607 injected with 1 mg 40H-TAM at 15-19 weeks and compared to four similarly treated *Sox10-CreER*^{T2};
608 *RdT* mice (three female, one male) and one female *Pik3ca*$^{fl(H1047R)/+}$ controls of the same age. Within

bioRxiv preprint doi: https://doi.org/10.1101/2022.04.05.487130; this version posted April 6, 2022. The copyright holder for this preprint (which was not certified by peer review) is the author/funder, who has granted bioRxiv a license to display the preprint in perpetuity. It is made available under aCC-BY-ND 4.0 International license.

609 five days, one mutant had died and the three others had attained a humane endpoint and were
610 euthanized. Cause of death was not determined, but gross examination of the *Sox10-CreER*^{T2}; *RdT*
611 mice under a fluorescence binocular dissecting microscope demonstrated effective recombination had
612 been induced in all. Although no obvious tumors had developed in the mutants, the superficially
613 pigmented axillary and Peyer's patch lymph nodes had enlarged germinal centers (not shown), and
614 the ovaries were lumpy (**Figure 7**(**F**)).

615 *Sox10-CreER*^{T2} males were then mated to three *Pik3ca*$^{flox(1047R)/+}$ females and the pregnant dams
616 treated at E18.5 with 4OH-TAM to induce recombination in post-migratory NC and other Sox10-
617 expressing cells just before birth. This led to recovery of a total of ten live births: five *Sox10-*
618 *CreER*^{T2}; *Pik3ca*$^{H1047R/+}$ (three female, two male), four *Sox10-CreER*^{T2} and one male *Pik3ca*$^{H1047R/+}$
619 mouse. These animals were followed without incident for up to 1 year, when one male mutant rapidly
620 developed an unpigmented, circumscribed tail tumor of 5 mm in diameter and showed signs of
621 distress. After euthanasia, the tumor could be seen to contain varied cellular elements including
622 smooth muscle and mucin-containing myxoid zones that stained with Alcian blue (**Figure 7**(**G**)).
623 (A) Extracutaneous pigmented melanocyte deposits along nerves and muscle fascia in *Krox20-*
624 *Cre*$^{+/\circ}$; *Pik3ca*$^{H1047R/+}$ mice, close to vascular anomalies. Bar = 2 mm.
625 (B) Increased meningeal melanocytosis over ventromedial frontal lobes and olfactory bulbs in
626 *Krox20-Cre*$^{+/\circ}$; *Pik3ca*$^{H1047R/+}$ mutants, not seen in 4OH-TAM-treated *Sox10-Cre*$^{+/\circ}$; *Pik3ca*$^{H1047R/+}$
627 mice. Bar = 2 mm.
628 (C) Pigmented, gingival melanocytosis over lower incisors of *Krox20-Cre*$^{+/\circ}$; *Pik3ca*$^{H1047R/+}$ mutants,
629 not seen in 4OH-TAM-treated *Sox10-Cre*$^{+/\circ}$; *Pik3ca*$^{H1047R/+}$ mice. Bar = 1 mm.
630 (D) Melanoma in *Krox20-Cre*$^{+/\circ}$; *Pik3ca*$^{H1047R/+}$ mutant mouse near seminal gland. Bar = 2 mm.
631 (E) Rhabdomyomatous mesenchymal hamartoma in thigh of *Krox20-Cre*$^{+/\circ}$; *Pik3ca*$^{H1047R/+}$ mutant
632 mouse. Bar = 100 µm.
633 (F) Ovary of *Sox10-CreER*^{T2}; *Pik3ca*$^{H1047R/+}$ mouse induced at 15 weeks with 1 mg 4OH-TAM, after
634 5 days.
635 (G) Unpigmented, myxoid melanoma in tail of induced *Sox10-CreER*^{T2}; *Pik3ca*$^{H1047R/+}$ mouse, after
636 nearly one year. Bar = 100 µm.

637 ## 7 Conflict of Interest

638 The authors declare that the research was conducted in the absence of any commercial or financial
639 relationships that could be construed as a potential conflict of interest.

640 ## 8 Author Contributions

641 EM, MM and ML planned and performed mouse crosses and dissections, and undertook the
642 histology and immunofluorescence experiments as well as microscopy. AP contributed the data for
643 Figure 2. GM and AB provided reagents and expertise on PI3K signaling. TF dissected pituitary
644 glands and aided in the interpretation of the pituitary sections. NM reviewed the histology. HCE
645 contributed the *in situ* hybridization and microscopy, conducted statistical analyses, obtained funding
646 and wrote the manuscript. All authors reviewed the final manuscript.

647 ## 9 Funding

648 A travel grant from CREST-NET to A.P. seeded this collaboration. Further funding for this work was
649 provided by patient advocacy groups: Association Française contre les Myopathies (MoThARD
650 project), the Association du Naevus Géant Congénital, Asociación Española de Nevus Gigante

bioRxiv preprint doi: https://doi.org/10.1101/2022.04.05.487130; this version posted April 6, 2022. The copyright holder for this preprint (which was not certified by peer review) is the author/funder, who has granted bioRxiv a license to display the preprint in perpetuity. It is made available under aCC-BY-ND 4.0 International license.

651 Congénito, the Association Naevus 2000 France-Europe and the Blackswan Foundation (RE(ACT)
652 CMN).

653 ## 10 Acknowledgments

654 The authors acknowledge all the members of the DIP-NET team for ensuring continuity under
655 challenging circumstances. They also thank A. Ghata and the rest of the MMG animal platform for
656 their precious assistance, and L. Slimani for help generating the micro-CT data at the PIV core
657 facility (http://piv.parisdescartes.fr/).

658 ## 11 Contribution to the field statement

659 In this paper, my co-authors and I have developed multiple new mouse models to test the
660 developmental function of a gene whose mutations are frequent and well known to cancer
661 researchers, called PIK3CA. One particular mutation is present in 4 out of 10 common malignancies
662 due to this gene, permanently activating the enzyme that it encodes and driving aggressive tumor
663 growth. We have carefully observed and described the anatomical and molecular characteristics of
664 the many malformations that can also be caused by the same oncogenic mutation. Mutations of
665 PIK3CA have also been identified over the last decade in numerous rare disease syndromes with
666 overlapping symptoms, among which musculoskeletal, brain and vascular malformations are
667 regularly observed. By restricting PIK3CA activity to specific subsets of cells in the mouse, we have
668 identified that their abilities to make or influence other cell types renders them more vulnerable to
669 causing changes in tissue shape and size, or to developing cancer. These mouse models indicate
670 additional candidate diseases in humans where PIK3CA may be locally active, opening new potential
671 applications for existing treatments.

672 ## 12 References

673 Adameyko, I., Lallemend, F., Aquino, J. B., Pereira, J. A., Topilko, P., Müller, T., et al. (2009).
674 Schwann Cell Precursors from Nerve Innervation Are a Cellular Origin of Melanocytes in Skin.
675 *Cell* 139, 366–379. doi:10.1016/j.cell.2009.07.049.

676 Adams, J. R., Xu, K., Liu, J. C., Agamez, N. M. R., Loch, A. J., Wong, R. G., et al. (2011).
677 Cooperation between Pik3ca and p53 Mutations in Mouse Mammary Tumor Formation. *Cancer*
678 *Res.* 71, 2706–2717. doi:10.1158/0008-5472.CAN-10-0738.

679 Alcantara, D., Timms, A. E., Gripp, K., Baker, L., Park, K., Collins, S., et al. (2017). Mutations of
680 AKT3 are associated with a wide spectrum of developmental disorders including extreme
681 megalencephaly. *Brain* 140, 2610–2622. doi:10.1093/brain/awx203.

682 Baggiolini, A., Callahan, S. J., Montal, E., Weiss, J. M., Trieu, T., Tagore, M. M., et al. (2021).
683 Developmental chromatin programs determine oncogenic competence in melanoma. *Science*
684 *(80-.).* 373. doi:10.1126/science.abc1048.

685 Bergwerff, M., Verberne, M. E., DeRuiter, M. C., Poelmann, R. E., and Gittenberger-de Groot, A. C.
686 (1998). Neural crest cell contribution to the developing circulatory system: implications for
687 vascular morphology? *Circ. Res.* 82, 221–31.

688 Bolande, R. P. (1974). The neurocristopathies: a unifying concept of disease arising in neural crest
689 development. *Hum. Pathol.* 5, 409–429.

bioRxiv preprint doi: https://doi.org/10.1101/2022.04.05.487130; this version posted April 6, 2022. The copyright holder for this preprint (which was not certified by peer review) is the author/funder, who has granted bioRxiv a license to display the preprint in perpetuity. It is made available under aCC-BY-ND 4.0 International license.

690 Canaud, G., Hammill, A. M., Adams, D., Vikkula, M., and Keppler-Noreuil, K. M. (2021). A review
691 of mechanisms of disease across PIK3CA-related disorders with vascular manifestations.
692 *Orphanet J. Rare Dis.* 16, 306. doi:10.1186/s13023-021-01929-8.

693 Castel, P., Carmona, F. J., Grego-Bessa, J., Berger, M. F., Viale, A., Anderson, K. V., et al. (2016).
694 Somatic PIK3CA mutations as a driver of sporadic venous malformations. *Sci. Transl. Med.* 8,
695 332ra42. doi:10.1126/scitranslmed.aaf1164.

696 Castillo, S. D., Tzouanacou, E., Zaw-Thin, M., Berenjeno, I. M., Parker, V. E. R., Chivite, I., et al.
697 (2016). Somatic activating mutations in Pik3ca cause sporadic venous malformations in mice
698 and humans. *Sci. Transl. Med.* 8, 332ra43-332ra43. doi:10.1126/scitranslmed.aad9982.

699 Ciarlo, C., Kaufman, C. K., Kinikoglu, B., Michael, J., Yang, S., D'Amato, C., et al. (2017). A
700 chemical screen in zebrafish embryonic cells establishes that Akt activation is required for
701 neural crest development. *Elife* 6, 1–26. doi:10.7554/eLife.29145.001.

702 Couto, J. A., Konczyk, D. J., Vivero, M. P., Kozakewich, H. P. W., Upton, J., Fu, X., et al. (2017).
703 Somatic PIK3CA mutations are present in multiple tissues of facial infiltrating lipomatosis.
704 *Pediatr. Res.* 82, 850–854. doi:10.1038/pr.2017.155.

705 Danielian, P. S., Muccino, D., Rowitch, D. H., Michael, S. K., and McMahon, a P. (1998).
706 Modification of gene activity in mouse embryos in utero by a tamoxifen-inducible form of Cre
707 recombinase. *Curr. Biol.* 8, 1323–6.

708 Deal, K. K., Rosebrock, J. C., Eeds, A. M., DeKeyser, J. M. L., Musser, M. A., Ireland, S. J., et al.
709 (2021). Sox10-cre BAC transgenes reveal temporal restriction of mesenchymal cranial neural
710 crest and identify glandular Sox10 expression. *Dev. Biol.* 471, 119–137.
711 doi:10.1016/j.ydbio.2020.12.006.

712 Dill, P. E., De Bernardis, G., Weber, P., and L??sch, U. (2014). Topical everolimus for facial
713 angiofibromas in the tuberous sclerosis complex. A first case report. *Pediatr. Neurol.* 51, 109–
714 113. doi:10.1016/j.pediatrneurol.2014.02.016.

715 Ding, H., Wu, X., Bostrom, H., Kim, I., Wong, N., Tsoi, B., et al. (2004). A specific requirement for
716 PDGF-C in palate formation and PDGFR-alpha signaling. *Nat Genet* 36, 1111–1116.

717 Etchevers, H. C., Dupin, E., and Le Douarin, N. M. (2019). The diverse neural crest: from
718 embryology to human pathology. *Development* 146, 0–3. doi:10.1242/dev.169821.

719 Etchevers, H. C., Vincent, C., Le Douarin, N. M., and Couly, G. F. (2001). The cephalic neural crest
720 provides pericytes and smooth muscle cells to all blood vessels of the face and forebrain.
721 *Development* 128, 1059–68.

722 Etchevers, H., Couly, G., Vincent, C., and Le Douarin, N. M. (1999). Anterior cephalic neural crest
723 is required for forebrain viability. *Development* 126, 3533–3543.

724 Frisk, S., Taylan, F., Blaszczyk, I., Nennesmo, I., Annerén, G., Herm, B., et al. (2019). Early
725 activating somatic PIK3CA mutations promote ectopic muscle development and upper limb
726 overgrowth. *Clin. Genet.* 96, 118–125. doi:10.1111/cge.13543.

bioRxiv preprint doi: https://doi.org/10.1101/2022.04.05.487130; this version posted April 6, 2022. The copyright holder for this preprint (which was not certified by peer review) is the author/funder, who has granted bioRxiv a license to display the preprint in perpetuity. It is made available under aCC-BY-ND 4.0 International license.

727 Gresset, A., Coulpier, F., Gerschenfeld, G., Jourdon, A., Matesic, G., Richard, L., et al. (2015).
728 Boundary Caps Give Rise to Neurogenic Stem Cells and Terminal Glia in the Skin. *Stem Cell*
729 *Reports* 5, 278–290. doi:10.1016/j.stemcr.2015.06.005.

730 Gudjohnsen, S. A. H., Atacho, D. A. M., Gesbert, F., Raposo, G., Hurbain, I., Larue, L., et al. (2015).
731 Meningeal Melanocytes in the Mouse: Distribution and Dependence on Mitf. *Front. Neuroanat.*
732 9, 149. doi:10.3389/fnana.2015.00149.

733 He, F., and Soriano, P. (2013). A Critical Role for PDGFRα Signaling in Medial Nasal Process
734 Development. *PLoS Genet.* 9. doi:10.1371/journal.pgen.1003851.

735 Ho, A. C. C., Liu, A. P. Y., Lun, K. S., Tang, W. F., Chan, K. Y. K., Lau, E. Y. T., et al. (2012).
736 European Journal of Medical Genetics A newborn with a 790 kb chromosome 17p13 . 3
737 microduplication presenting with aortic stenosis , microcephaly and dysmorphic facial features e
738 Is cardiac assessment necessary for all patients with 17p13 . 3 microduplica. *Eur. J. Med. Genet.*
739 55, 758–762. doi:10.1016/j.ejmg.2012.09.011.

740 Hong, T., Xiao, X., Ren, J., Cui, B., Zong, Y., Zou, J., et al. (2021). Somatic MAP3K3 and PIK3CA
741 mutations in sporadic cerebral and spinal cord cavernous malformations. *Brain* 144, 2648–2658.
742 doi:10.1093/brain/awab117.

743 Hori, Y., Hirose, K., Aramaki-Hattori, N., Suzuki, S., Nakayama, R., Inoue, M., et al. (2020). Fibro-
744 adipose vascular anomaly (FAVA): three case reports with an emphasis on the mammalian
745 target of rapamycin (mTOR) pathway. *Diagn. Pathol.* 15, 98. doi:10.1186/s13000-020-01004-z.

746 Jiang, X., Iseki, S., Maxson, R. E., Sucov, H. M., and Morriss-Kay, G. M. (2002). Tissue origins and
747 interactions in the mammalian skull vault. *Dev Biol* 241, 106–116.

748 Juriloff, D. M., and Harris, M. J. (2008). Mouse Genetic Models of Cleft Lip with or without Cleft
749 Palate. *Teratology* 77, 63–77. doi:10.1002/bdra.20430.

750 Kaucka, M., Szarowska, B., Kavkova, M., Kastriti, M. E., Kameneva, P., Schmidt, I., et al. (2021).
751 Nerve-associated Schwann cell precursors contribute extracutaneous melanocytes to the heart,
752 inner ear, supraorbital locations and brain meninges. *Cell. Mol. Life Sci.* 78, 6033–6049.
753 doi:10.1007/s00018-021-03885-9.

754 Keppler-Noreuil, K. M., Sapp, J. C., Lindhurst, M. J., Parker, V. E. R., Blumhorst, C., Darling, T., et
755 al. (2014). Clinical delineation and natural history of the PIK3CA-related overgrowth spectrum.
756 *Am. J. Med. Genet.* 164, 1713–33. doi:10.1002/ajmg.a.36552.

757 Kingsmore, S., Smith, L., Soden, S., Dinwiddie, D., Saunders, C., Farrow, E., et al. (2013). Exome
758 Sequencing Reveals De Novo Germline Mutation of the Mammalian Target of Rapamycin
759 (MTOR) in a Patient with Megalencephaly and Intractable Seizures. *J. Genomes Exomes*, 63.
760 doi:10.4137/JGE.S12583.

761 Krings, T., Geibprasert, S., Luo, C. B., Bhattacharya, J. J., Alvarez, H., and Lasjaunias, P. (2007).
762 Segmental neurovascular syndromes in children. *Neuroimaging Clin. N. Am.* 17, 245–58.
763 doi:10.1016/j.nic.2007.02.006.

764 Kurek, K. C., Howard, E., Tennant, L. B., Upton, J., Alomari, A. I., Burrows, P. E., et al. (2012).

bioRxiv preprint doi: https://doi.org/10.1101/2022.04.05.487130; this version posted April 6, 2022. The copyright holder for this preprint (which was not certified by peer review) is the author/funder, who has granted bioRxiv a license to display the preprint in perpetuity. It is made available under aCC-BY-ND 4.0 International license.

765 PTEN hamartoma of soft tissue: a distinctive lesion in PTEN syndromes. *Am. J. Surg. Pathol.*
766 36, 671–87. doi:10.1097/PAS.0b013e31824dd86c.

767 Le Douarin, N., and Kalcheim, C. (1999). *The Neural Crest*. 2nd ed. Cambridge, U.K.: Cambridge
768 University Press.

769 Le Lièvre, C. S. (1978). Participation of neural crest-derived cells in the genesis of the skull in birds.
770 *J. Embryol. Exp. Morphol.* 47, 17–37. doi:10.1007/978-90-481-3375-8_4.

771 Le Lievre, C. S., and Le Douarin, N. M. (1975). Mesenchymal derivatives of the neural crest:
772 analysis of chimaeric quail and chick embryos. *J. Embryol. Exp. Morphol.* 34, 125–154.

773 Lee, J. H., Huynh, M., Silhavy, J. L., Kim, S., Dixon-Salazar, T., Heiberg, A., et al. (2012). De novo
774 somatic mutations in components of the PI3K-AKT3-mTOR pathway cause
775 hemimegalencephaly. *Nat. Genet.* 44, 941–945. doi:10.1038/ng.2329.

776 Lian, C. G., Sholl, L. M., Zakka, L. R., O, T. M., Liu, C., Xu, S., et al. (2014). Novel Genetic
777 Mutations in a Sporadic Port-Wine Stain. *JAMA Dermatology* 150, 1336.
778 doi:10.1001/jamadermatol.2014.1244.

779 Limaye, N., Kangas, J., Mendola, A., Godfraind, C., Schlögel, M. J., Helaers, R., et al. (2015).
780 Somatic Activating PIK3CA Mutations Cause Venous Malformation. *Am. J. Hum. Genet.* 97,
781 914–921. doi:10.1016/j.ajhg.2015.11.011.

782 Luks, V. L., Kamitaki, N., Vivero, M. P., Uller, W., Rab, R., Bovée, J. V. M. G., et al. (2015).
783 Lymphatic and Other Vascular Malformative/Overgrowth Disorders Are Caused by Somatic
784 Mutations in PIK3CA. *J. Pediatr.* 166, 1048-1054.e5. doi:10.1016/j.jpeds.2014.12.069.

785 Madisen, L., Zwingman, T. A., Sunkin, S. M., Oh, S. W., Zariwala, H. A., Gu, H., et al. (2010). A
786 robust and high-throughput Cre reporting and characterization system for the whole mouse
787 brain. *Nat. Neurosci.* 13, 133–40. doi:10.1038/nn.2467.

788 Marek, T., Mahan, M. A., Carter, J. M., Howe, B. M., Bartos, R., Amrami, K. K., et al. (2021).
789 What's known and what's new in adipose lesions of peripheral nerves? *Acta Neurochir. (Wien).*
790 163, 835–842. doi:10.1007/s00701-020-04620-2.

791 Maro, G. S., Vermeren, M., Voiculescu, O., Melton, L., Cohen, J., Charnay, P., et al. (2004). Neural
792 crest boundary cap cells constitute a source of neuronal and glial cells of the PNS. *Nat.*
793 *Neurosci.* 7, 930–8. doi:10.1038/nn1299.

794 Mendiratta, G., Ke, E., Aziz, M., Liarakos, D., Tong, M., and Stites, E. C. (2021). Cancer gene
795 mutation frequencies for the U.S. population. *Nat. Commun.* 12, 5961. doi:10.1038/s41467-021-
796 26213-y.

797 Muhl, L., Genové, G., Leptidis, S., Liu, J., He, L., Mocci, G., et al. (2020). Single-cell analysis
798 uncovers fibroblast heterogeneity and criteria for fibroblast and mural cell identification and
799 discrimination. *Nat. Commun.* 11, 1–18. doi:10.1038/s41467-020-17740-1.

800 Müller, S. M., Stolt, C. C., Terszowski, G., Blum, C., Amagai, T., Kessaris, N., et al. (2008). Neural
801 crest origin of perivascular mesenchyme in the adult thymus. *J. Immunol.* 180, 5344–51.

bioRxiv preprint doi: https://doi.org/10.1101/2022.04.05.487130; this version posted April 6, 2022. The copyright holder for this preprint (which was not certified by peer review) is the author/funder, who has granted bioRxiv a license to display the preprint in perpetuity. It is made available under aCC-BY-ND 4.0 International license.

802 doi:10.4049/jimmunol.180.8.5344.

803 Odelin, G., Faure, E., Coulpier, F., Di Bonito, M., Bajolle, F., Studer, M., et al. (2018). Krox20
804 defines a subpopulation of cardiac neural crest cells contributing to arterial valves and bicuspid
805 aortic valve. *Development* 145, dev151944. doi:10.1242/dev.151944.

806 Ola, R., Dubrac, A., Han, J., Zhang, F., Fang, J. S., Larrivée, B., et al. (2016). PI3 kinase inhibition
807 improves vascular malformations in mouse models of hereditary haemorrhagic telangiectasia.
808 *Nat. Commun.* 7, 13650. doi:10.1038/ncomms13650.

809 Orr-Urtreger, A., Bedford, M. T., Do, M. S., Eisenbach, L., and Lonai, P. (1992). Developmental
810 expression of the α receptor for platelet-derived growth factor, which is deleted in the
811 embryonic lethal Patch mutation. *Development* 115, 289–303. doi:10.1242/dev.115.1.289.

812 Petersen, J., and Adameyko, I. (2017). Nerve-associated neural crest: peripheral glial cells generate
813 multiple fates in the body. *Curr. Opin. Genet. Dev.* 45, 10–14. doi:10.1016/j.gde.2017.02.006.

814 Pilatti, P., and Astúa, D. (2017). Orbit orientation in didelphid marsupials (Didelphimorphia:
815 Didelphidae). *Curr. Zool.* 63, 403–415. doi:10.1093/cz/zow068.

816 Ren, A. A., Snellings, D. A., Su, Y. S., Hong, C. C., Castro, M., Tang, A. T., et al. (2021). PIK3CA
817 and CCM mutations fuel cavernomas through a cancer-like mechanism. *Nature* 594, 271–276.
818 doi:10.1038/s41586-021-03562-8.

819 Roy, A., Skibo, J., Kalume, F., Ni, J., Rankin, S., Lu, Y., et al. (2015). Mouse models of human
820 PIK3CA-related brain overgrowth have acutely treatable epilepsy. *Elife* 4, 1–25.
821 doi:10.7554/eLife.12703.

822 Segrelles, C., Moral, M., Lorz, C., Santos, M., Lu, J., Cascallana, J. L., et al. (2008). Constitutively
823 active Akt induces ectodermal defects and impaired bone morphogenetic protein signaling. *Mol.*
824 *Biol. Cell* 19, 137–49. doi:10.1091/mbc.e07-08-0764.

825 Shirley, M. D., Tang, H., Gallione, C. J., Baugher, J. D., Frelin, L. P., Cohen, B., et al. (2013).
826 Sturge-Weber syndrome and port-wine stains caused by somatic mutation in GNAQ (SI). *N.*
827 *Engl. J. Med.* 368, 1971–9. doi:10.1056/NEJMoa1213507.

828 Sittewelle, M., and Monsoro-Burq, A. H. (2018). AKT signaling displays multifaceted functions in
829 neural crest development. *Dev. Biol.* 444, S144–S155. doi:10.1016/j.ydbio.2018.05.023.

830 Stone, L. S. (1926). Further experiments on the extirpation and transplantation of mesectoderm in
831 Amblystoma punctatum. *J. Exp. Zool.* 44, 95–131.

832 Tachibana, N., Touahri, Y., Dixit, R., David, L. A., Adnani, L., Cantrup, R., et al. (2018).
833 Hamartoma-like lesions in the mouse retina: an animal model of Pten hamartoma tumour
834 syndrome. *Dis. Model. Mech.* 11, dmm031005. doi:10.1242/dmm.031005.

835 Tallquist, M. D., and Soriano, P. (2003). Cell autonomous requirement for PDGFRalpha in
836 populations of cranial and cardiac neural crest cells. *Development* 130, 507–518.
837 doi:10.1242/dev.00241.

bioRxiv preprint doi: https://doi.org/10.1101/2022.04.05.487130; this version posted April 6, 2022. The copyright holder for this preprint (which was not certified by peer review) is the author/funder, who has granted bioRxiv a license to display the preprint in perpetuity. It is made available under aCC-BY-ND 4.0 International license.

838 Tan, W.-H., Baris, H. N., Burrows, P. E., Robson, C. D., Alomari, A. I., Mulliken, J. B., et al. (2007).
839 The spectrum of vascular anomalies in patients with PTEN mutations: implications for diagnosis
840 and management. *J. Med. Genet.* 44, 594–602. doi:10.1136/jmg.2007.048934.

841 Thomas, A. C., Heux, P., Santos, C., Arulvasan, W., Solanky, N., Carey, M. E., et al. (2018).
842 Widespread dynamic and pleiotropic expression of the melanocortin-1-receptor (MC1R) system
843 is conserved across chick, mouse and human embryonic development. *Birth Defects Res.* 110,
844 443–455. doi:10.1002/bdr2.1183.

845 Topilko, P. (2019). Neural crest derived boundary cap cells: A source of pericytes to the developing
846 peripheral vasculature. *Morphologie* 103, 71–72. doi:10.1016/j.morpho.2019.10.007.

847 Venot, Q., Blanc, T., Rabia, S. H., Berteloot, L., Ladraa, S., Duong, J. P., et al. (2018). Targeted
848 therapy in patients with PIK3CA-related overgrowth syndrome. *Nature* 558, 540–546.
849 doi:10.1038/s41586-018-0217-9.

850 Voiculescu, O., Charnay, P., and Schneider-Maunoury, S. (2000). Expression pattern of a Krox-
851 20/Cre knock-in allele in the developing hindbrain, bones, and peripheral nervous system.
852 *Genesis* 26, 123–126. doi:10.1002/(SICI)1526-968X(200002)26:2<123::AID-
853 GENE7>3.0.CO;2-O.

854 Watt, K. E. N., and Trainor, P. A. (2014). “Neurocristopathies: The Etiology and Pathogenesis of
855 Disorders Arising from Defects in Neural Crest Cell Development,” in *Neural Crest Cells:*
856 *Evolution, Development and Disease*, 361–394. doi:http://dx.doi.org/10.1016/B978-0-12-
857 401730-6.00018-1.

858 Wiszniak, S., Mackenzie, F. E., Anderson, P., Kabbara, S., Ruhrberg, C., and Schwarz, Q. (2015).
859 Neural crest cell-derived VEGF promotes embryonic jaw extension. *Proc. Natl. Acad. Sci.* 112,
860 201419368. doi:10.1073/pnas.1419368112.

861 Xie, M., Kamenev, D., Kaucka, M., Kastriti, M. E., Zhou, B., Artemov, A. V., et al. (2019). Schwann
862 cell precursors contribute to skeletal formation during embryonic development in mice and
863 zebrafish. *Proc. Natl. Acad. Sci. U. S. A.* 116, 15068–15073. doi:10.1073/pnas.1900038116.

864 Zachariah, M. A., and Cyster, J. G. (2010). Neural Crest-Derived Pericytes Promote Egress of
865 Mature Thymocytes at the Corticomedullary Junction. *Science (80-.).* 328, 1129–1135.
866 doi:10.1126/science.1188222.

867

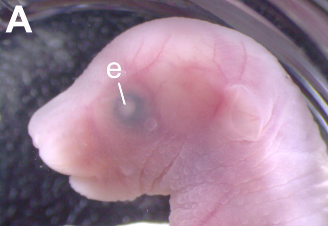
A
e
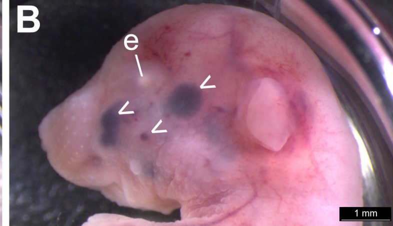
B
e
1 mm
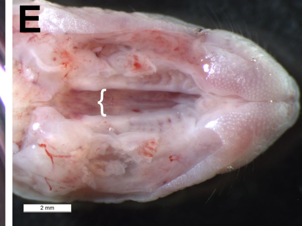
E
2 mm
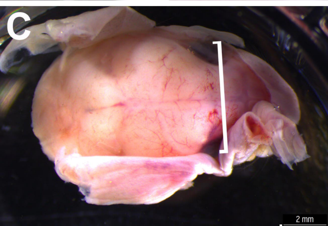
C
2 mm
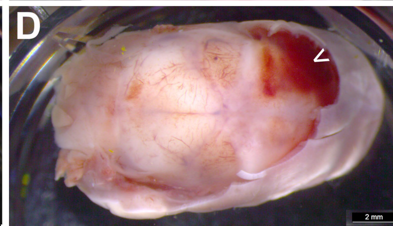
D
2 mm
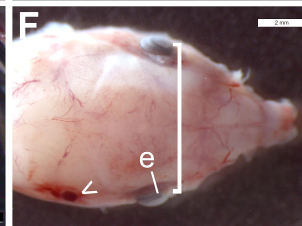
F
2 mm
e
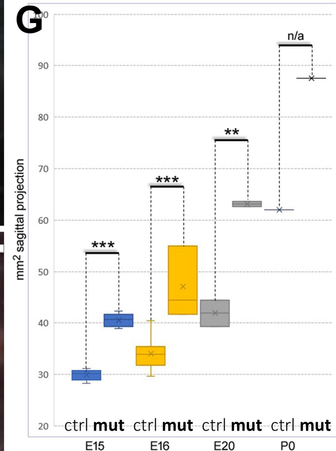
G
mm2 sagital projection
100
90
80
70
60
50
40
30
20
***
***
**
n/a
ctrl mut
ctrl mut
ctrl mut
ctrl mut
E15
E16
E20
P0

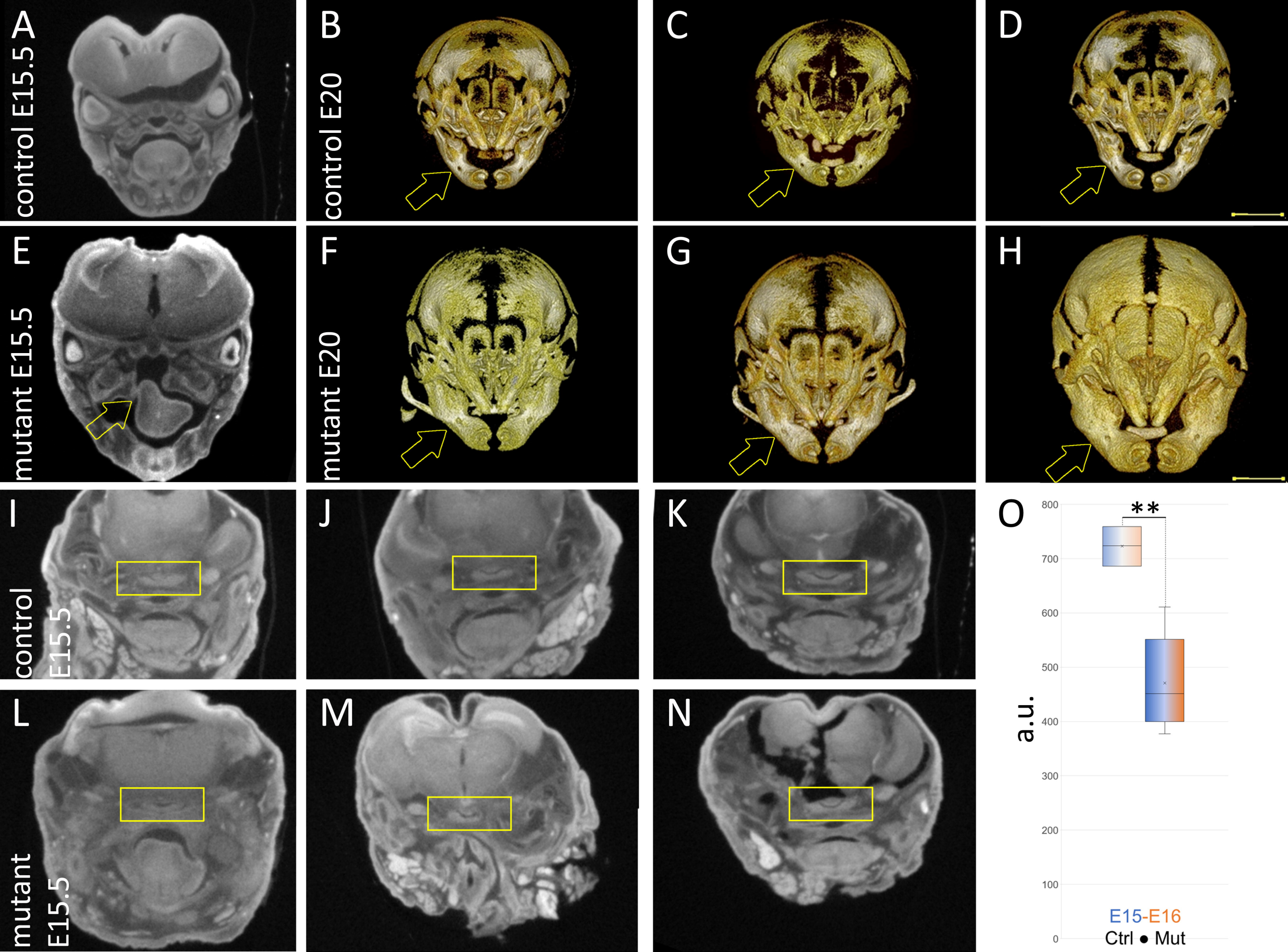
A
control E15.5
B
control E20
C
D
E
mutant E15.5
F
mutant E20
G
H
I
control E15.5
J
K
L
mutant E15.5
M
N
O
**
800
700
600
500
400
300
200
100
0
a.u.
E15-E16
Ctrl ● Mut

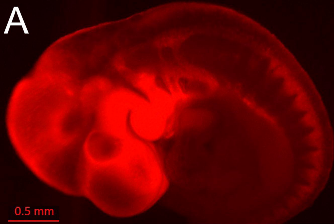
A
0.5 mm
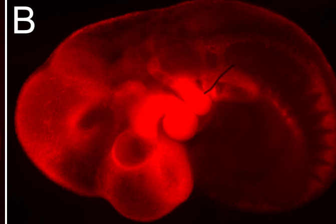
B
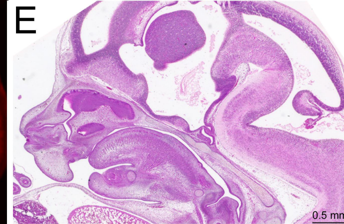
E
0.5 mm
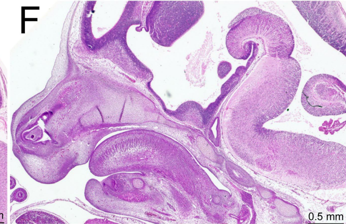
F
0.5 mm
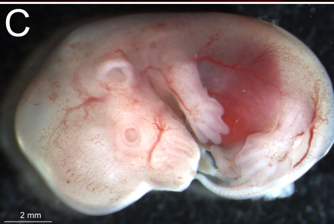
C
2 mm

D
2 mm
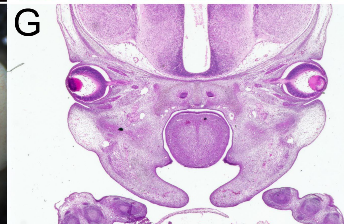
G
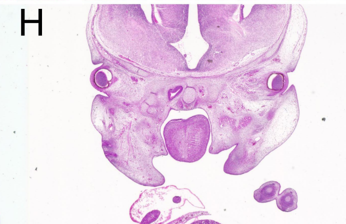
H
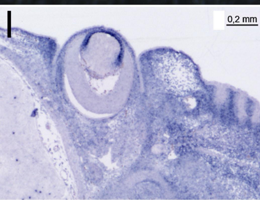
I
0,2 mm
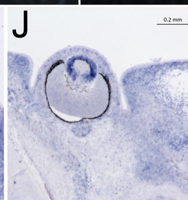
J
0.2 mm
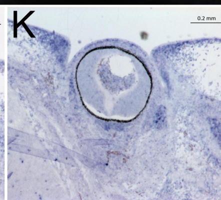
K
0.2 mm
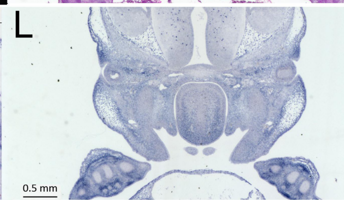
L
0.5 mm
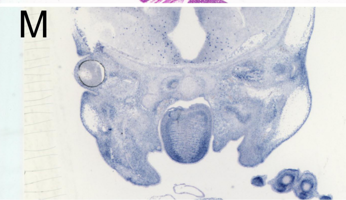
M

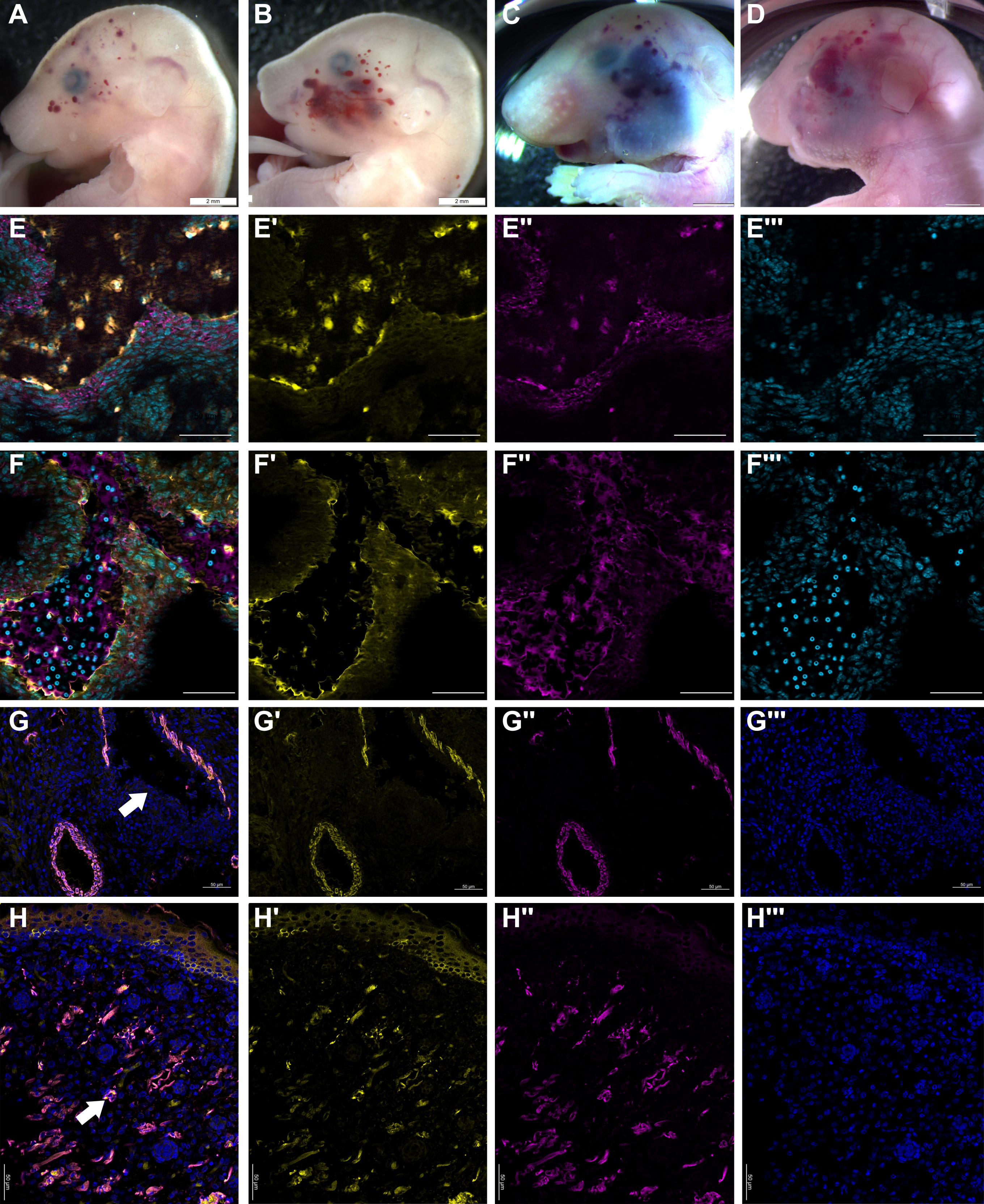
A
2 mm
B
2 mm
C
D
E
E'
E''
E'''
F
F'
F''
F'''
G
50 µm
G'
50 µm
G''
50 µm
G'''
50 µm
H
50 µm
H'
50 µm
H''
50 µm
H'''
50 µm

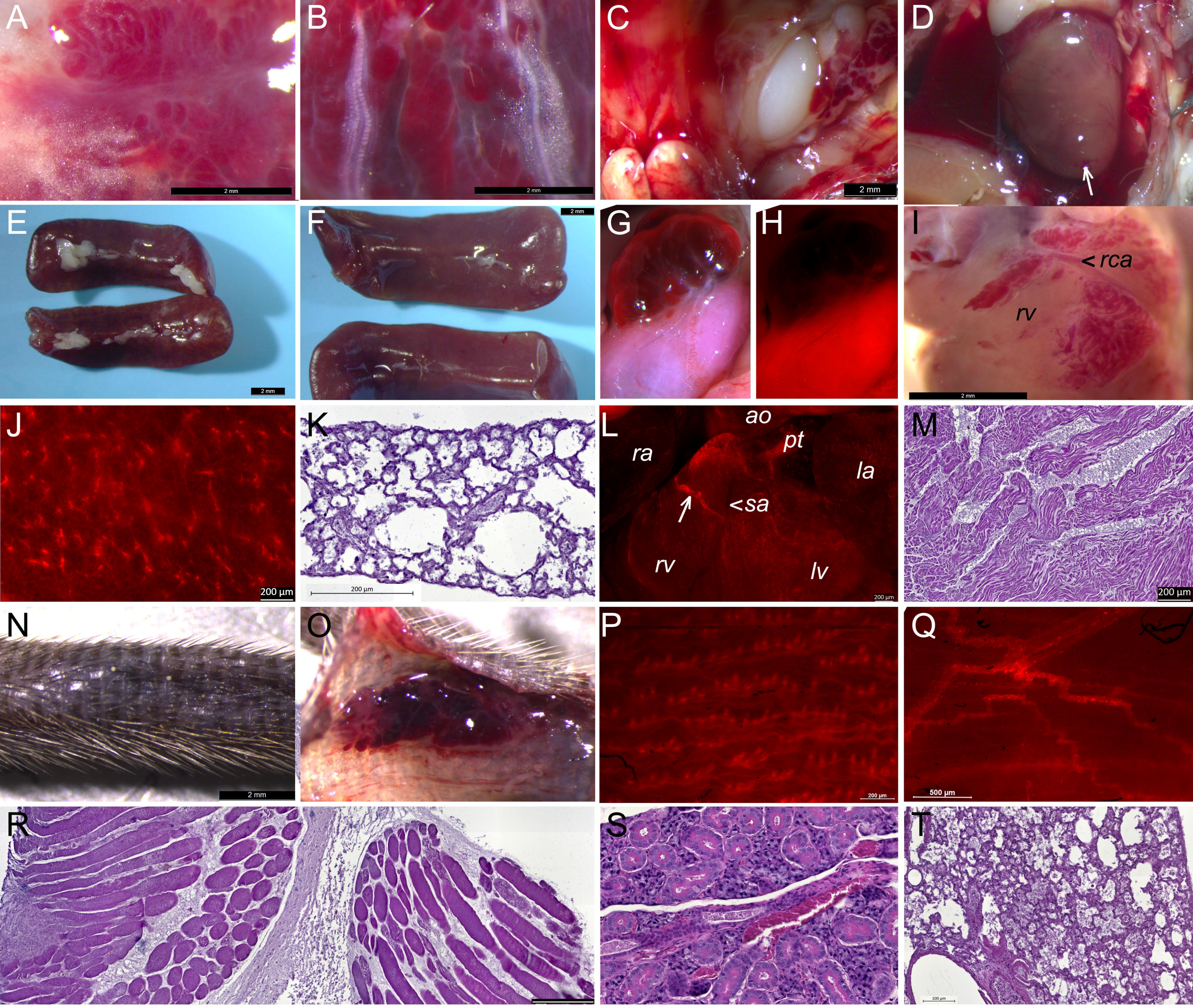
A
2 mm
B
2 mm
C
2 mm
D
E
2 mm
F
2 mm
G
H
I
< rca
rv
2 mm
J
200 µm
K
200 µm
L
ao
pt
ra
la
<sa
rv
lv
200 µm
M
200 µm
N
2 mm
O
P
200 µm
Q
500 µm
R
S
T
100 µm

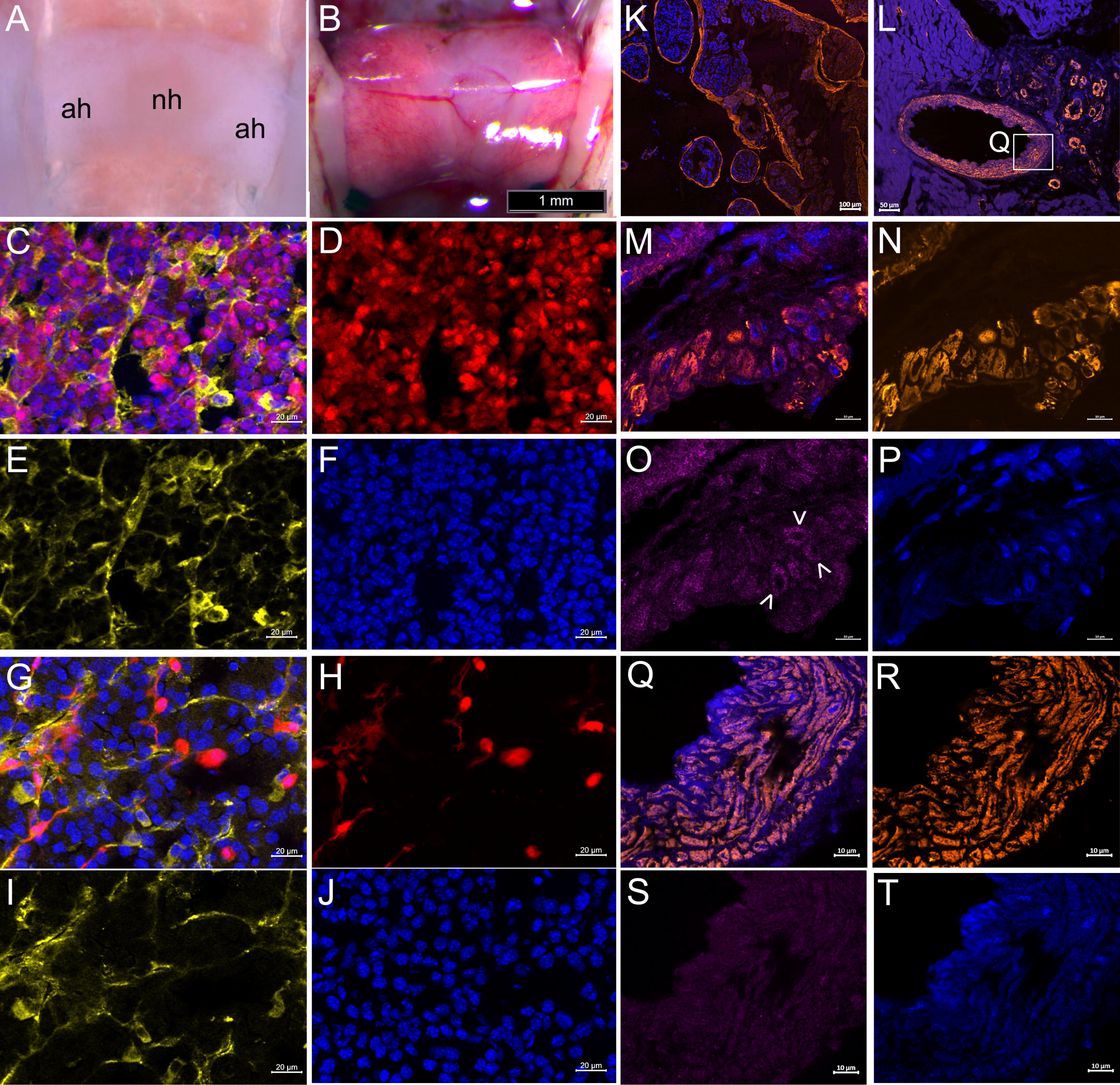
A
ah
nh
ah
B
1 mm
K
100 µm
L
Q
50 µm
C
20 µm
D
20 µm
M
10 µm
N
10 µm
E
20 µm
F
20 µm
O
10 µm
P
10 µm
G
20 µm
H
20 µm
Q
10 µm
R
10 µm
I
20 µm
J
20 µm
S
10 µm
T
10 µm

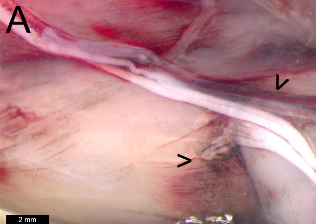
A
2 mm
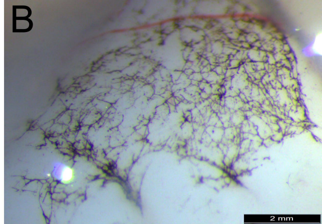
B
2 mm
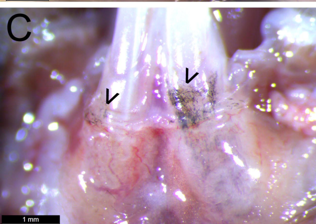
C
1 mm
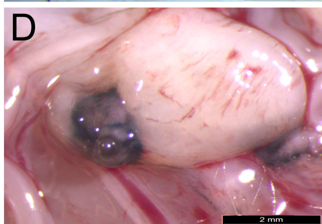
D
2 mm
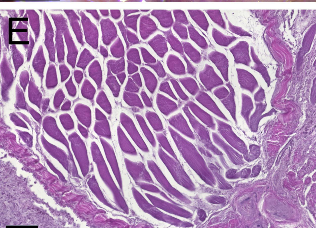
E
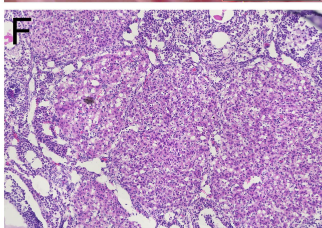
F
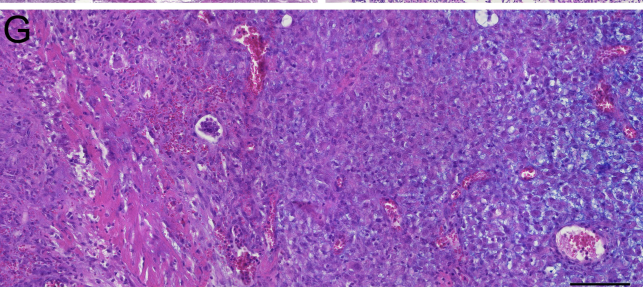
G